Measurement of the production cross-sections of $\pi^{\pm}$ in p-C and $\pi^{\pm}$-C interactions at 12 GeV/c

HARP Collaboration

February 20, 2013

Abstract

The results of the measurements of the double-differential production cross-sections of pions, $d^2\sigma^\pi/dpd\Omega$, in p-C and $\pi^{\pm}$-C interactions using the forward spectrometer of the HARP experiment are presented. The incident particles are 12 GeV/c protons and charged pions directed onto a carbon target with a thickness of 5% of a nuclear interaction length. For p-C interactions the analysis is performed using 100 035 reconstructed secondary tracks, while the corresponding numbers of tracks for π^--C and π^+-C analyses are 106 534 and 10 122 respectively. Cross-section results are presented in the kinematic range 0.5 GeV/$c \le p_\pi < 8$ GeV/c and 30 mrad $\le \theta_\pi < 240$ mrad in the laboratory frame. The measured cross-sections have a direct impact on the precise calculation of atmospheric neutrino fluxes and on the improved reliability of extensive air shower simulations by reducing the uncertainties of hadronic interaction models in the low energy range.

HARP collaboration

M.G. Catanesi, E. Radicioni

Università degli Studi e Sezione INFN, Bari, Italy

R. Edgecock, M. Ellis[1], S. Robbins[2,3], F.J.P. Soler[4]

Rutherford Appleton Laboratory, Chilton, Didcot, UK

C. Gößling

Institut für Physik, Universität Dortmund, Germany

S. Bunyatov, A. Krasnoperov, B. Popov[5], V. Tereshchenko

Joint Institute for Nuclear Research, JINR Dubna, Russia

E. Di Capua, G. Vidal–Sitjes[6]

Università degli Studi e Sezione INFN, Ferrara, Italy

A. Artamonov[7], S. Giani, S. Gilardoni, P. Gorbunov[7], A. Grant, A. Grossheim[10], P. Gruber[11], V. Ivanchenko[12], A. Kayis-Topaksu[13], J. Panman, I. Papadopoulos, E. Tcherniaev, I. Tsukerman[7], R. Veenhof, C. Wiebusch[14], P. Zucchelli[9,15]

CERN, Geneva, Switzerland

A. Blondel, S. Borghi[16], M. Campanelli, M.C. Morone[17], G. Prior[18], R. Schroeter

Section de Physique, Université de Genève, Switzerland

R. Engel, C. Meurer

Forschungszentrum Karlsruhe, Institut für Kernphysik, Karlsruhe, Germany

I. Kato[10,20]

University of Kyoto, Japan

U. Gastaldi

Laboratori Nazionali di Legnaro dell' INFN, Legnaro, Italy

G. B. Mills[20]

Los Alamos National Laboratory, Los Alamos, USA

J.S. Graulich[21], G. Grégoire

Institut de Physique Nucléaire, UCL, Louvain-la-Neuve, Belgium

M. Bonesini, F. Ferri

Università degli Studi e Sezione INFN, Milano, Italy

M. Kirsanov

Institute for Nuclear Research, Moscow, Russia

A. Bagulya, V. Grichine, N. Polukhina

P. N. Lebedev Institute of Physics (FIAN), Russian Academy of Sciences, Moscow, Russia

V. Palladino

Università "Federico II" e Sezione INFN, Napoli, Italy

L. Coney[21], D. Schmitz[21]

Columbia University, New York, USA

G. Barr, A. De Santo[22], C. Pattison, K. Zuber[23]

Nuclear and Astrophysics Laboratory, University of Oxford, UK

F. Bobisut, D. Gibin, A. Guglielmi, M. Mezzetto

Università degli Studi e Sezione INFN, Padova, Italy

J. Dumarchez, F. Vannucci

LPNHE, Universités de Paris VI et VII, Paris, France

U. Dore

Università "La Sapienza" e Sezione INFN Roma I, Roma, Italy

D. Orestano, F. Pastore, A. Tonazzo, L. Tortora

Università degli Studi e Sezione INFN Roma III, Roma, Italy

C. Booth, L. Howlett

Dept. of Physics, University of Sheffield, UK

M. Bogomilov, M. Chizhov, D. Kolev, R. Tsenov

Faculty of Physics, St. Kliment Ohridski University, Sofia, Bulgaria

S. Piperov, P. Temnikov

Institute for Nuclear Research and Nuclear Energy, Academy of Sciences, Sofia, Bulgaria

M. Apollonio, P. Chimenti, G. Giannini, G. Santin[24]

Università degli Studi e Sezione INFN, Trieste, Italy

J. Burguet–Castell, A. Cervera–Villanueva, J.J. Gómez–Cadenas, J. Martín–Albo, P. Novella, M. Sorel

Instituto de Física Corpuscular, IFIC, CSIC and Universidad de Valencia, Spain

[1]Now at FNAL, Batavia, Illinois, USA.

[2]Jointly appointed by Nuclear and Astrophysics Laboratory, University of Oxford, UK.

[3]Now at Codian Ltd., Langley, Slough, UK.

[4]Now at University of Glasgow, UK.

[5]Also supported by LPNHE, Universités de Paris VI et VII, Paris, France.

[6]Now at Imperial College, University of London, UK.

[7]ITEP, Moscow, Russian Federation.

[8]Permanently at Instituto de Física de Cantabria, Univ. de Cantabria, Santander, Spain.

[9]Now at SpinX Technologies, Geneva, Switzerland.

[10]Now at TRIUMF, Vancouver, Canada.

[11]Now at University of St. Gallen, Switzerland.

[12]On leave of absence from Ecoanalitica, Moscow State University, Moscow, Russia.

[13]Now at Çukurova University, Adana, Turkey.

[14]Now at III Phys. Inst. B, RWTH Aachen, Aachen, Germany.

[15]On leave of absence from INFN, Sezione di Ferrara, Italy.

[16]Now at CERN, Geneva, Switzerland.

[17]Now at Univerity of Rome Tor Vergata, Italy.

[18]Now at Lawrence Berkeley National Laboratory, Berkeley, California, USA.

[19]K2K Collaboration.

[20]MiniBooNE Collaboration.

[21]Now at Section de Physique, Université de Genève, Switzerland, Switzerland.

[22]Now at Royal Holloway, University of London, UK.

[23]Now at University of Sussex, Brighton, UK.

[24]Now at ESA/ESTEC, Noordwijk, The Netherlands.

1   Introduction

The HARP experiment [1, 2] at the CERN PS was designed to make measurements of hadron yields from a large range of nuclear targets and for incident particle momenta from 1.5 GeV/c to 15 GeV/c. The main motivations are the measurement of pion yields for a quantitative design of the proton driver of a future neutrino factory [3], a substantial improvement in the calculation of the atmospheric neutrino fluxes [4] and the measurement of particle yields as input for the flux calculation of accelerator neutrino experiments, such as K2K [5, 6], MiniBooNE [7] and SciBooNE [8].

The first HARP physics publication [9] reported measurements of the π^+ production cross-section from an aluminum target at 12.9 GeV/c proton momentum. This corresponds to the energy of the KEK PS and the target material used by the K2K experiment. The results obtained in Ref. [9] were subsequently applied to the final neutrino oscillation analysis of K2K [6], allowing a significant reduction of the dominant systematic error associated with the calculation of the so-called far-to-near ratio (see [9] and [6] for a detailed discussion) and thus an increased K2K sensitivity to the oscillation signal.

Our next goal was to contribute to the understanding of the MiniBooNE and SciBooNE neutrino fluxes. They are both produced by the Booster Neutrino Beam at Fermilab which originates from protons accelerated to 8.9 GeV/c by the booster before being collided against a beryllium target. As was the case for the K2K beam, a fundamental input for the calculation of the resulting neutrino flux is the measurement of the π^+ production cross-sections from a beryllium target at 8.9 GeV/c proton momentum, which is presented in [10].

We have also performed measurements with the HARP detector of the double-differential cross-section for $\pi^\pm$ production at large angles by protons in the momentum range of 3–12.9 GeV/c impinging on different thin 5% nuclear interaction length (λ_I) targets [12, 13, 14]. These measurements are of special interest for target materials used in conventional accelerator neutrino beams and in neutrino factory designs.

In this paper we address one of the other main motivations of the HARP experiment: the measurement of the yields of positive and negative pions relevant for a precise calculation of the atmospheric neutrino fluxes and improved modeling of extended air showers (EAS). We present measurements of the double-differential cross-section, $\mathrm{d}^2\sigma^\pi/\mathrm{d}p\mathrm{d}\Omega$ for $\pi^\pm$ production (in the kinematic range 0.5 GeV/$c \leq p_\pi < 8$ GeV/c and 30 mrad $\leq \theta_\pi < 240$ mrad) by protons and charged pions of 12 GeV/c momentum impinging on a thin carbon target of 5% λ_I. These measurements are performed using the forward spectrometer of the HARP detector. HARP results on the measurement of the double-differential $\pi^\pm$ production cross-section in proton–carbon collisions in the range of pion momentum 100 MeV/$c \leq p_\pi < 800$ MeV/c and angle 0.35 rad $\leq \theta_\pi < 2.15$ rad obtained with the HARP large-angle spectrometer are presented in a separate article [13].

The existing world data for $\pi^\pm$ production on light targets in the low energy region of incoming beam ($\leq$25 GeV) are rather limited. A number of fixed target measurements with a good phase space coverage exist for beryllium targets and low energy proton beams [15, 16, 17, 18, 19, 20]. However, in general these data are often restricted to a few fixed angles and have limited statistics. The work of Eichten et al. [19] has become a widely used standard reference dataset. This experiment used a proton beam with energy of 24 GeV and a beryllium target. The secondary particles (pions, kaons, protons) were measured in a broad angular range (17 mrad $< \theta < 127$ mrad) and in momentum region from 4 GeV/c up to 18 GeV/c. A measurement of inclusive pion production in proton-beryllium interactions at 6.4, 12.3, and 17.5 GeV/c proton beam momentum has been published recently by the E910 experiment at BNL [21]. In this work the differential π^+ and π^- production cross-sections have been measured up to 400 mrad in θ_π and up to 6 GeV/c in p_π. We should stress, however, that the data for pion projectiles are still very scarce.
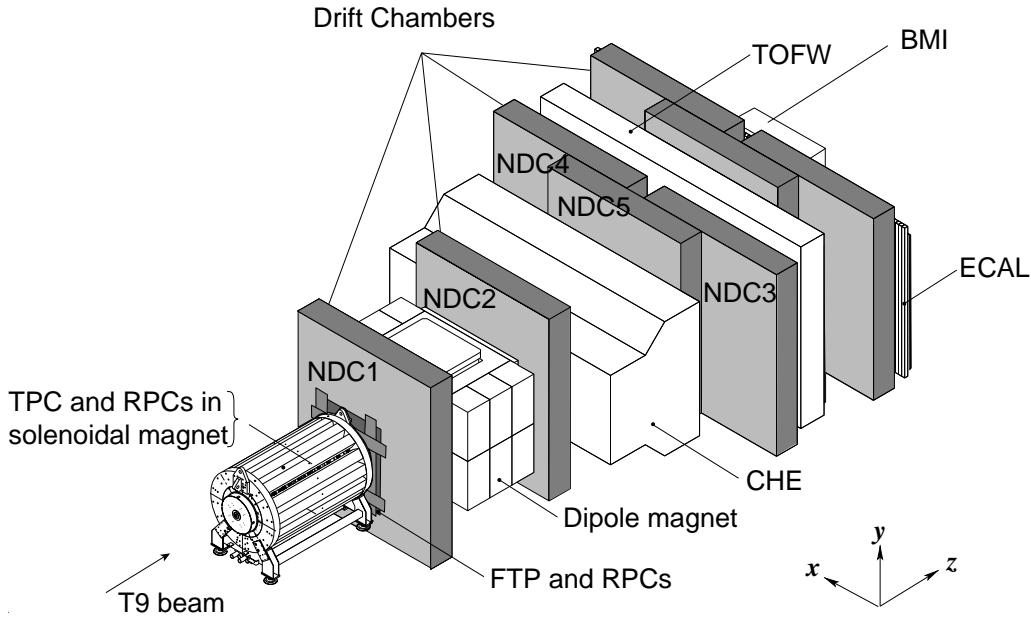
Figure 1: Schematic layout of the HARP detector. The convention for the coordinate system is shown in the lower-right corner.

Carbon is isoscalar and so are nitrogen and oxygen, so the extrapolation to air is the most straightforward. Unfortunately, the existing data for a carbon target at low energies are very scarce. The only measurement of p-C collisions, which was not limited to a fixed angle, was the experiment done by Barton et al. [22]. These data were collected using the Fermilab Single Arm Spectrometer facility in the M6E beam line. A proton beam with a momentum of 100 GeV/c and a thin 2% λ_I (1.37 g/cm^2) carbon target was used. However, the phase space of the secondary particles (pions, kaons, protons) covers only a very small part of the phase space of interest to the calculation of the atmospheric neutrino fluxes and to EAS modeling.

Recently the p-C data at 158 GeV/c provided by the NA49 experiment at CERN SPS in a large acceptance range have become available [23]. The relevant data are expected also from the MIPP experiment at Fermilab [24]. We would like to mention that the NA61 experiment [25] took first p-C data at 30 GeV/c in autumn of 2007. The foreseen measurements of importance for astroparticle physics are studies of p-C interactions at the incoming beam momenta 30, 40, 50 GeV/c and $\pi^{\pm}$-C interactions at 158 and 350 GeV/c.

1.1   Experimental apparatus

The HARP experiment [1, 2] makes use of a large-acceptance spectrometer consisting of a forward and large-angle detection system. The HARP detector is shown in Fig. 1. A detailed description of the experimental apparatus can be found in Ref. [2]. The forward spectrometer is based on five modules of large area drift chambers (NDC1-5) [26] and a dipole magnet complemented by a set of detectors for particle identification (PID): a time-of-flight wall (TOFW) [27], a large Cherenkov detector (CHE) and an electromagnetic calorimeter (ECAL). It covers polar angles up to 250 mrad. The muon contamination of the beam is measured with a muon identifier consisting of thick iron absorbers and scintillation counters. The large-angle spectrometer – based on a Time Projection Chamber (TPC) and Resistive Plate Chambers (RPCs) located inside a solenoidal magnet – has a large acceptance in the momentum and angular range for the pions relevant to the production of the muons in a neutrino factory (see the corresponding HARP publications [12, 13, 14]). For the analysis described here we use the forward spectrometer and the beam instrumentation.
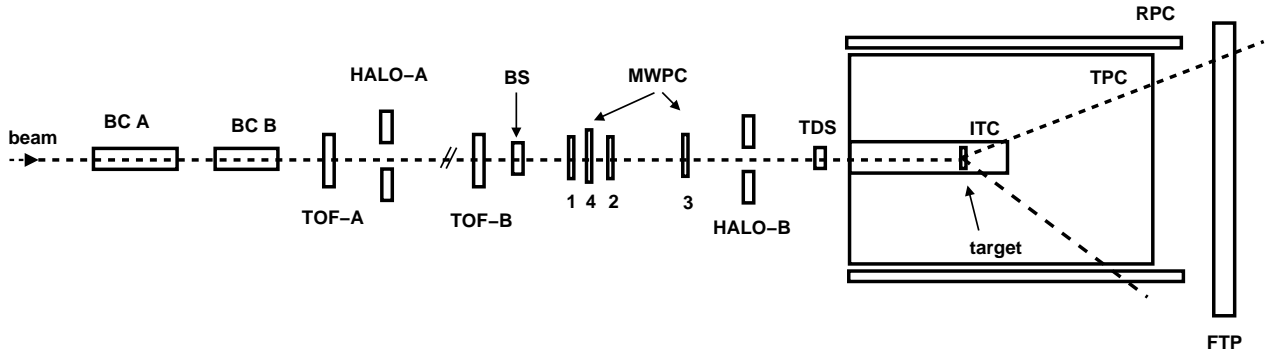
Figure 2: Schematic view of the trigger and beam equipment. The description is given in the text. The beam enters from the left. The MWPCs are numbered: 1, 4, 2, 3 from left to right. On the right, the position of the target inside the inner field cage of the TPC is shown.

The HARP experiment, located in the T9 beam of the CERN PS, took data in 2001 and 2002. The momentum definition of the T9 beam is known with a precision of the order of 1% [28].

The target is placed inside the inner field cage (IFC) of the TPC. The cylindrical carbon target used for the measurements reported here has a purity of 99.99%, a thickness of 18.94 mm, a diameter of 30.26 mm and a mass of 25.656 g. The corresponding density of the target is 1.88 g/cm^3 (for comparison the density of graphite is 2.27 g/cm^3). The thickness of the carbon target is equivalent to 5% of a nuclear interaction length (3.56 g/cm^2).

A sketch of the equipment in the beam line is shown in Fig. 2. A set of four multi-wire proportional chambers (MWPCs) measures the position and direction of the incoming beam particles with an accuracy of ≈1 mm in position and ≈0.2 mrad in angle per projection. A beam time-of-flight system (BTOF) measures the time difference of particles over a 21.4 m path-length. It is made of two identical scintillation hodoscopes, TOFA and TOFB (originally built for the NA52 experiment [29]), which, together with a small target-defining trigger counter (TDS, also used for the trigger and described below), provide particle identification at low energies. This provides separation of pions, kaons and protons up to 5 GeV/c and determines the initial time at the interaction vertex (t_0). The timing resolution of the combined BTOF system is about 70 ps. A system of two N$_2$-filled Cherenkov detectors (BCA and BCB) is used to tag electrons at low energies and pions at higher energies. The electron and pion tagging efficiency is found to be close to 100%. At the beam energy used for this analysis the Cherenkov counters are used to descriminate between protons and lighter particles, while the BTOF is used to reject ions.

A set of trigger detectors completes the beam instrumentation: a thin scintillator slab covering the full aperture of the last quadrupole magnet in the beam line is used to start the trigger logic decision (BS); a small scintillator disk, TDS mentioned above, positioned upstream of the target to ensure that only particles hitting the target cause a trigger; and 'halo' counters (scintillators with a hole to let the beam particles pass) to veto particles too far away from the beam axis. The TDS is designed to have a very high efficiency (measured to be 99.9% [30]). The trigger signal was formed by a logical OR of four photo-multipliers which viewed the side of the disk from four sides through light-guides. The distribution of multiplicity of the signals of the four photo-multipliers could be used to infer the overall efficiency. It is located as near as possible to the entrance of the TPC and has a 20 mm diameter, smaller than the target diameter of 30 mm. Its time resolution (∼ 130 ps) is sufficiently good to be used as an additional detector for the BTOF system.

A downstream trigger in the forward trigger plane (FTP) was required to record the event. The FTP is a double plane of scintillation counters covering the full aperture of the spectrometer magnet except a 60 mm central hole for allowing non-interacting beam particles to pass. The efficiency is measured using tracks recognized by the pattern recognition in the NDC's in a sample of events taken with a beam-trigger only and with a trigger based on signals in the Cherenkov detector. Accepting only tracks with a trajectory outside the central hole, the efficiency of the FTP is measured to be >99.8%.

The track reconstruction and particle identification algorithms as well as the calculation of reconstruction efficiencies are described in details in [9, 10, 11].

1.2   Experimental techniques for the HARP forward spectrometer

A detailed description of established experimental techniques for the data analysis in the HARP forward spectrometer can be found in Ref. [9, 11].

With respect to our first published paper on pion production in p–Al interactions [9], a number of improvements to the analysis techniques and detector simulation have been made. The present results are based on the same event reconstruction as described in Ref. [10]. The most important improvements introduced in this analysis compared with the one presented in Ref. [9] are:

- An increase of the track reconstruction efficiency which is now constant over a much larger kinematic range and a better momentum resolution coming from improvements in the tracking algorithm.

- Better understanding of the momentum scale and resolution of the detector, based on data, which was then used to tune the simulation. The empty-target data (which is used as a "test beam" exposure for the dipole spectrometer), elastic scattering data using a liquid hydrogen target and a method of comparison with the measurement of the particle velocity in the TOFW were used to study the momentum calibration. This results in smaller systematic errors associated with the unsmearing corrections determined from the Monte Carlo simulation.

- New particle identification hit selection algorithms both in the TOFW and in the CHE resulting in much reduced background and negligible efficiency losses. The PID algorithms developed for the HARP forward spectrometer are described in details in Ref. [9, 11] and the recent improvements are reported in Ref. [10]. In the kinematic range of the current analysis, the pion identification efficiency is about 98%, while the background from mis-identified protons is well below 1%.

- Significant increases in Monte Carlo production have also reduced uncertainties from Monte Carlo statistics and allowed studies which have reduced certain systematics.

Further details of the improved analysis techniques can be found in [10]. For the current analysis we have used identical reconstruction and PID algorithms, while at the final stage of the analysis the unfolding technique introduced as UFO in [9] has been applied. The application of this technique has already been described in Ref. [12].

The absolute normalization of the number of incident protons was performed using 'incident-proton' triggers. These are triggers where the same selection on the beam particle was applied but no selection on the interaction was performed. The rate of this trigger was down-scaled by a factor 64.

The muon contamination in the beam was measured by the beam muon identifier (BMI) located downstream of the calorimeter (see Fig. 1). The BMI is a 1.40 m wide structure placed in the horizontal direction asymmetrically

with respect to the beamline, in order to intercept all the beam muons which are horizontally deflected by the spectrometer magnet. It consists of a passive 0.40 m layer of iron followed by an iron-scintillator sandwich with five planes of six scintillators each, read out at both sides, giving a total of 6.4 λ_{int}.

In section 2 we present the analysis procedure. Physics results are presented in section 3 together with a discussion on the relevance of these results to atmospheric neutrino flux calculations and to extensive air shower simulations. Finally, a summary is presented in section 4.

2 Analysis of charged pion production in p-C and $\pi^\pm$-C interactions

2.1 Data selection

The datasets used for the measurements of the production cross-sections of positive and negative pions in p-C and $\pi^\pm$-C interactions at 12 GeV/c were taken during two short run periods (only two days long for each beam polarity) in June and September 2002. Over one million events with positive beam and more than half a million events with negative beam were collected. For detailed event statistics see Table 1.

2.1.1 Beam particle selection and interaction selection

At the first stage of the analysis a favoured beam particle type is selected using the beam time of flight system (TOF-A, TOF-B) and the Cherenkov counters (BCA, BCB) as described in section 1.1. A value of the pulse height consistent with the pedestal in both beam Cherenkov detectors distinguishes protons from electrons and pions. We also ask for time measurements in TOF-A, TOF-B and/or TDS which are needed for calculating the arrival time of the beam proton at the target. The beam TOF system is used to reject ions, such as deuterons, but at 12 GeV/c is not used to separate protons from pions.

The set of criteria for selecting beam protons for this analysis is as follows: we require ADC counts to be less than 130 in BCA and less than 125 in BCB (see [2, 9] for more details). The beam pions are selected by applying cuts on the ADC counts in BCA and BCB to be outside the range accepted for protons in both Cherenkov counters.

In the 12 GeV/c beam setting the nitrogen pressure in the beam Cherenkov counters was too low for kaons to be above the threshold. Kaons are thus a background to the proton sample. However, the fraction of kaons has been measured in the 12.9 GeV/c beam configuration which is expected to be very similar to the beam used in the present measurement. In the 12.9 GeV/c beam the fraction of kaons compared to protons was found to be 0.5%. Electrons radiate in the Cherenkov counters and would be counted as pions. In the 3 GeV/c beam electrons are identified by both BCA and BCB, since the pressure was such that pions remained below threshold. In the 5 GeV/c beam electrons could be tagged by BCB only; in BCA pions were already above threshold. The e/π fraction was measured to be 1% in the 3 GeV/c beam and $< 10^{-3}$ in the 5 GeV/c beam. By extrapolation from the lower-energy beam settings this electron contamination can be estimated to be negligible ($< 10^{-3}$).

In addition to the momentum-selected beam of protons and pions originating from the T9 production target one expects also the presence of muons from pion decay both downstream and upstream of the beam momentum selection. Therefore, precise absolute knowledge of the pion rate incident on the HARP targets is required when measurements of particle production with incident pions are performed. The particle identification detectors in the beam do not distinguish muons from pions. A separate measurement of the muon component has been performed using datasets without target ("empty-target datasets") both for Monte Carlo and real data. Since

the empty-target data were taken with the same beam parameter settings as the data taken with targets, the beam composition can be measured in the empty-target runs and then used as an overall correction for the counting of pions in the runs with targets.

Muons are recognized by their longer range in the BMI. The punch-through background in the BMI is measured counting the protons (identified with the beam detectors) thus mis-identified as muons by the BMI. A comparison of the punch-through rate between simulated incoming pions and protons was used to determine a correction for the difference between pions and protons and to determine the systematic error. This difference is the dominant systematic error in the beam composition measurement. The aim was to determine the composition of the beam as it strikes the target, thus muons produced in pion decays after the HARP target should be considered as a background to the measurement of muons in the beam. The rate of these background muons, which depends mainly on the total inelastic cross-section and pion decay, was calculated by a Monte Carlo simulation using GEANT4 [31]. The muon fraction in the beam (at the target) is obtained taking into account the efficiency of the BMI selection criteria as well as the punch-through and decay backgrounds. The result of this analysis for the 12 GeV/c beam is $R = \mu/(\mu + \pi) = (2.8 \pm 1.0)\%$, where the quoted error includes both statistical and systematic errors.

Summarizing, the purity of the proton beam is better than 99%, with the main background formed by kaons estimated to be 0.5%. This impurity is neglected in the analysis. The pion beam has a negligible electron contamination and a muon contamination of almost 3%. The muon contamination is taken into account in the normalization of the pion beam.

The distribution of the position of beam particles reconstructed in MWPCs and extrapolated to the target is shown in Fig. 3. The position of the positive-charge selected beam is shifted by about 5 mm in the y-direction with respect to the nominal position ($x = 0; y = 0$) and covers a circular area of about 8 mm in diameter. In the case of negatively charged beam particles the beam hits the target more centrally but it has a broader distribution of about 14 mm width in the y-direction. The distributions shown in Fig. 3 are obtained using "unbiased" beam triggers where the requirement of the TDS hit and the veto in the halo counters are not applied. Also no requirement on an interaction seen in the spectrometers was made. Under these conditions the full width of the beam is recorded including particles which would not hit the target. The latter are removed by the standard selection criteria. To keep the selection efficiency high and to exclude interactions at the target edge only the beam particles within a radius of 12 mm with respect to the nominal beam axis are accepted for the analysis. In addition, the MWPC track is required to have a measured direction within 5 mrad of the nominal beam direction to further reduce halo particles. After these criteria the remaining number of events for datasets with positive and negative beam are summarized in Table 1. At 12 GeV/c the negative beam consists only of e^- and π^- (with a dominant fraction of π^-), while the positive beam is dominated by protons (with a small admixture of π^+). This explains a significantly different statistics of the π^--C and π^+-C datasets. Note that in the analysis the measured beam profiles are used in the MC simulations.

2.1.2 Secondary track selection

Secondary track selection criteria are optimized to ensure the quality of momentum reconstruction and a clean time-of-flight measurement while maintaining a high reconstruction efficiency. There are two kinds of acceptance criteria concerning the track reconstruction quality and the characteristics of the tracks relative to the geometry of the forward spectrometer. These criteria are described in what follows and a summary of track statistics for the three different datasets (p-C, π^+-C, π^--C) is given in Table 2. About 5% to 6% of all reconstructed tracks in accepted events are used for the final analysis. The sample of reconstructed tracks contains also large-angle and/or low momentum tracks which are only seen in the drift chamber module upstream of the dipole magnet.
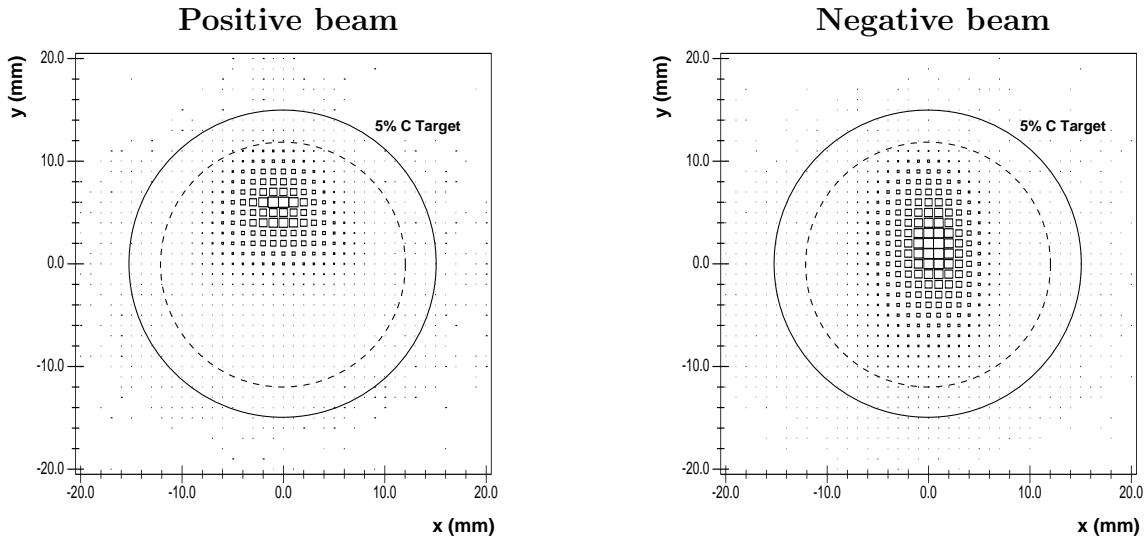
Positive beam

Negative beam

Figure 3: Reconstructed position of positively (left panel) and negatively (right panel) charged beam particles at the target plane. The solid circle gives the position and size of the carbon target (diameter: 30.26 mm), the dashed circle indicates the region which corresponds to the accepted beam particles (diameter: 24 mm).

Table 1: Total number of events in 12 GeV/c carbon target and empty target datasets and in corresponding Monte Carlo simulations (see section 2.4). The total number also includes triggers taken for normalization, calibration and for cross-section measurements in the large-angle spectrometer.

Selection	Carbon data	Empty target data	Monte Carlo
Positive beam	1 062 k	886 k	
p-C	467 k	287 k	20.3 M
π^+-C	40 k	25 k	20.8 M
Negative beam	646 k	531 k	
π^--C	350 k	214 k	20.8 M

The following reconstruction quality criteria have been applied:

- Successful momentum reconstruction of secondary particle (momentum estimator p_2, see Ref. [9] for details). The above momentum measurement is obtained by extrapolating the segment of the track downstream of the dipole magnet to the point defined by the position where the beam particle track traverses the longitudinal mid-plane of the target. Thus the position of the hits measured in the upstream drift chamber (NDC1) is not used for the momentum reconstruction.

- More than three hits on the track in NDC2 and at least five hits in a road around the particle trajectory [1] in one of the drift chamber modules NDC3, 4, or 5 or at least three hits on the track in one of the modules NDC3, 4, 5 and more than five hits in a road around the particle trajectory in NDC2.

- A loose criterion requiring more than three hits in a road around the trajectory in NDC1 and average $\chi^2 \leq 30$ for these hits with respect to the track in NDC1 in order to reduce non-target interaction

---

[1] The algorithm looks for drift chamber hits in a tube around the trajectory and places a cut on the matching χ^2.

Table 2: Number of tracks in accepted events before and after the selection criteria for secondary tracks are applied. About 5% to 6% of all tracks are used for the final analysis.

Selection	Number of reconstructed tracks	Number of selected tracks
p-C	2 057 420	100 035
π^+-C	192 976	10 122
π^--C	1 701 041	106 534

backgrounds.

- The track has a matched TOFW hit. Hits are matched based on the χ^2 of the extrapolation of the trajectory to the TOFW. When more particles share the same TOFW hit, the hit is assigned to the track with the best matching χ^2. When more TOFW hits are consistent with the trajectory, the one with the earliest time measurement is chosen. Hits have to pass a minimum pulse height requirement in the photo-multipliers on both ends of the scintillator to be accepted.

The criteria on track geometry are:

- The angle θ of a secondary particle with respect to the beam axis is required to be less than 300 mrad. The distribution of θ is shown in Fig. 4 (left panel). Only tracks with $\theta < 240$ mrad are retained in the final analysis.

- The y-component θ_y of the angle θ is required to be between -100 mrad and 100 mrad, see Fig. 4 (right panel). This cut is imposed by the vertical dipole magnet aperture[2].

- The extrapolation of a secondary track should point to the nominal beam axis on the target plane within a radius of 200 mm.

- Only tracks which bend towards the beam axis are accepted as shown in Fig. 5. This is the case if the product of charge and θ_x is negative. This criterion is applied to avoid the positive θ_x region for positively charged secondary particles and the negative θ_x region for negatively charged particles where the efficiency is momentum dependent due to the defocusing effect of the dipole magnet (see [9] for more details).

2.2   Empty target subtraction

There is a background induced by interactions of beam particles in the materials outside the target. This background is measured experimentally by taking data without a target in the target holder. These measurements are called "empty target data". The "empty target data" are also subject to the event and track selection criteria like the standard carbon datasets. The event statistics of these data samples are given in Table 1.

To take into account this background the number of particles of the observed type (π^+, π^-) in the "empty target data" are subtracted bin-by-bin (momentum and angular bins) from the number of particles of the same type in the carbon data. The average empty-target subtraction amounts to $\approx$20%. The uncertainty induced by this method is discussed in section 2.5 and labeled "empty target subtraction".

---

[2]In previous publications, the more conservative requirement -80 mrad $\leq \theta_y \leq 80$ mrad was applied. No degradation of efficiency, momentum resolution and PID performance was observed in the larger vertical angle acceptance region.
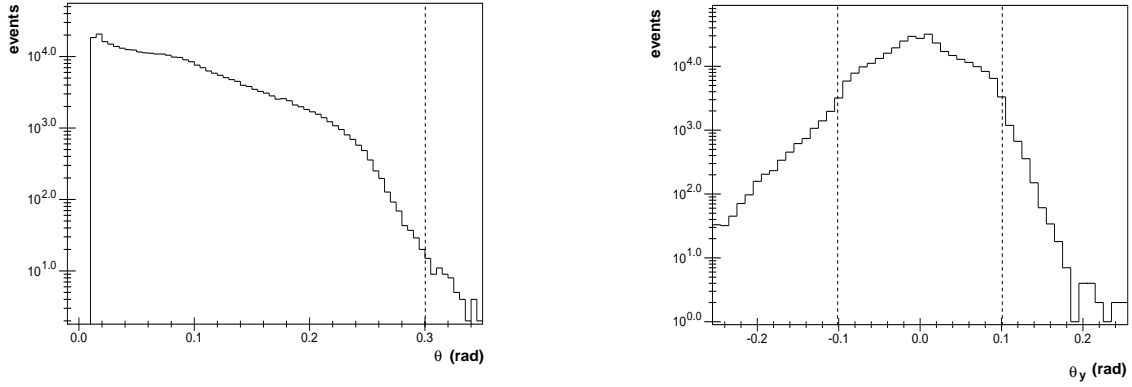
Figure 4: Distribution of θ (left panel) and θ_y (right panel) for reconstructed tracks. The acceptance criteria for these observables are indicated by dashed lines.
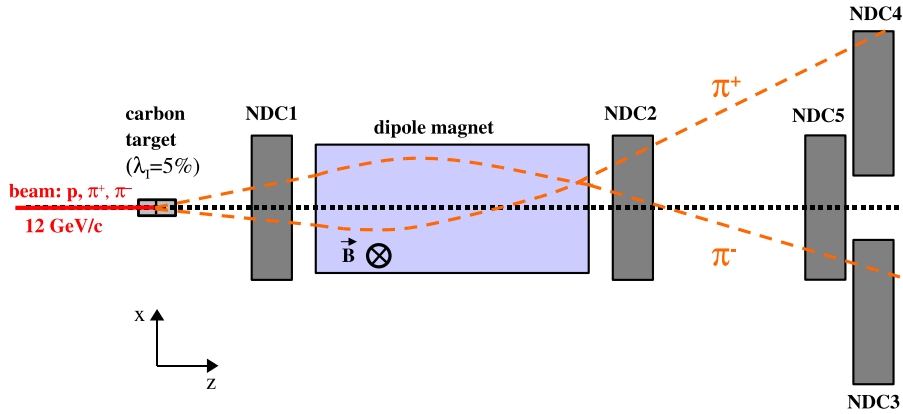

Figure 5: Top view of the HARP forward spectrometer. Only tracks which bend towards the beam axis are accepted. This means the product of charge and θ_x must be negative.

2.3   Calculation of cross-section

The goal of this analysis is to measure the double-differential inclusive production cross-section of negative and positive pions in p-C, π^+-C and π^--C interactions at 12 GeV/c in a broad range of secondary pion momentum and angle. The cross-section is calculated as follows

$$\frac{d^2\sigma^\alpha}{dpd\Omega}(p_i,\theta_j) \quad = \quad \frac{A}{N_A\rho t}\cdot\frac{1}{N_{\text{pot}}}\cdot\frac{1}{\Delta p_i\Delta\Omega_j}\cdot\sum_{p_i',\theta_j',\alpha'}\mathcal{M}^{\text{cor}}_{p_i\theta_j\alpha p_i'\theta_j'\alpha'}\cdot N^{\alpha'}(p_i',\theta_j')\,, \tag{1}$$

where

- $\frac{d^2\sigma^\alpha}{dpd\Omega}(p_i,\theta_j)$ is the cross-section in mb/(GeV/c sr) for the particle type α (p, π^+or π^-) for each momentum and angle bin (p_i,θ_j) covered in this analysis;

- $N^{\alpha'}(p_i',\theta_j')$ is the number of particles of type α in bins of reconstructed momentum p_i' and angle θ_j' in the raw data after empty target subtraction;

- $\mathcal{M}^{\text{cor}}_{p\theta\alpha p'\theta'\alpha'}$ is the correction matrix which accounts for efficiency and resolution of the detector;

- $\frac{A}{N_A\rho t}$, $\frac{1}{N_{\text{pot}}}$ and $\frac{1}{\Delta p_i\Delta\Omega_j}$ are normalization factors, namely:

    $\frac{N_A\rho t}{A}$ is the number of target nuclei per unit area [3];

    N_{pot} is the number of incident beam particles on target (particles on target);

    Δp_i and $\Delta\Omega_j$ are the bin sizes in momentum and solid angle, respectively [4].

We do not make a correction for the attenuation of the proton beam in the target, so that strictly speaking the cross-sections are valid for a $\lambda_{\text{I}} = 5\%$ target.

2.4   Calculation of the correction matrix

A calculation of the correction matrix $M^{\text{cor}}_{p_i\theta_j\alpha p_i'\theta_j'\alpha'}$ is a rather difficult task. Various techniques are described in the literature to obtain this matrix. As discussed in Ref. [9] for the p-Al analysis of HARP data at 12.9 GeV/c, two complementary analyses have been performed to cross-check internal consistency and possible biases in the respective procedures. A comparison of both analyses shows that the results are consistent within the overall systematic error [9].

In the first method – called "Atlantic" in [9] – the correction matrix $M^{\text{cor}}_{p_i\theta_j\alpha p_i'\theta_j'\alpha'}$ is decomposed into distinct independent contributions, which are computed mostly using the data themselves. The second method – called UFO in [9] – is the unfolding method introduced by D'Agostini [32]. It is based on the Bayesian unfolding technique. In this case a simultaneous (three dimensional) unfolding of momentum p, angle θ and particle type α is performed. The correction matrix is computed using a Monte Carlo simulation. This method has been used in recent HARP publications [12, 13, 14] and it is also applied in the analysis described here (see [33] for additional information).

---

[3]A - atomic mass, N_A - Avogadro number, ρ - target density and t - target thickness
[4]$\Delta p_i = p_i^{\text{max}} - p_i^{\text{min}}$, $\Delta\Omega_j = 2\pi(\cos(\theta_j^{\text{min}}) - \cos(\theta_j^{\text{max}}))$

2.4.1   Unfolding technique

Caused by various error sources (biases and resolutions) and limited acceptance and efficiency of an experiment, no measured observable represents the "true" physical value. The unfolding method tries to solve this problem and to find the corresponding true distribution from a distribution in the measured observable. The main assumption is that the probability distribution function in the "true" physical parameters can be approximated by a histogram with discrete bins. Then the relation between the vector $\vec{x}$ of the true physical parameter and the vector $\vec{y}$ of the measured observable can be described by a matrix $\mathcal{M}_{\mathrm{mig}}$ which represents the mapping from the true value to the measured one. This matrix is called the migration (or smearing) matrix

$$\vec{y} = \mathcal{M}_{\mathrm{mig}} \cdot \vec{x} \quad . \tag{2}$$

In our case these $\vec{x}$ and $\vec{y}$ vectors contain particle momentum, polar angle and particle type.

The goal of the unfolding procedure is to determine a transformation for the measurement to obtain the expected values for $\vec{x}$ using the relation (2), see e.g. [34]. The most simple and obvious solution is the matrix inversion. But this method often provides unstable results. Large correlations between bins lead to large off-diagonal elements in the migration matrix $\mathcal{M}_{\mathrm{mig}}$ and, thus, the result is dominated by very large variances and strong negative correlation between neighbouring bins.

In the method of D'Agostini [32], the unfolding is performed by the calculation of the unfolding matrix $\mathcal{M}^{\mathrm{UFO}} = \mathcal{M}^{\mathrm{cor}}$ in an iterative way which is used instead of $\mathcal{M}_{\mathrm{mig}}^{-1}$. Here $\mathcal{M}^{\mathrm{UFO}}$ is a two-dimensional matrix connecting the measurement space (effects) with the space of the true values (causes). Expected causes and measured effects are represented by one-dimensional vectors with entries $x_{\mathrm{exp}}(C_i)$ and $y(E_j)$ for each cause and effect bin C_i and E_j, respectively:

$$x_{\mathrm{exp}}(C_i) = \sum_j \mathcal{M}_{ij}^{\mathrm{UFO}} \ y(E_j) \quad . \tag{3}$$

The Bayes' theorem provides the conditional probability $P(C_i|E_j)$ for effect E_j to be caused by cause C_i

$$P(C_i|E_j) = P(E_j|C_i) \cdot P(C_i) \quad , \tag{4}$$

where $P(E_j|C_i)$ is the probability for cause C_i to produce effect E_j which corresponds to the migration matrix and could be calculated from Monte Carlo, $P(C_i)$ is the probability for cause C_i to happen. The Eq. (4) is solved in an iterative process. The initial probability $P_0(C_i)$ could be assumed to be a uniform distribution. The $P(C_i|E_j)$ found is used as the unfolding matrix in the first interaction step and leads to a first estimation of the expected values for causes

$$x_{\mathrm{exp}}(C_i) = \sum_j P(C_i|E_j) \ y(E_j) \quad . \tag{5}$$

From $x_{\mathrm{exp}}(C_i)$ a new probability $P_1(C_i)$ for cause C_i is calculated and inserted in Eq. (4) for the next iteration step. Before this, the distribution of $P_1(C_i)$ can optionally be smoothed to reduce oscillations due to statistical fluctuations. Between two consecutive iteration steps a χ^2-test is applied. The iteration process is terminated when the difference of χ^2 between consecutive iteration steps is small. This procedure was tested on distributions obtained with simulated data and verified to yield results consistent with the "true input" distributions. The final result of this method is the unfolded distribution of $x_{\mathrm{exp}}(C_i)$ and its covariance matrix. We have also checked that starting with flat priors at the first iteration does not introduce any biases in the final result.

The original unfolding program provided by D'Agostini is used in this analysis: $P_0(C_i)$ is assumed to be a uniform distribution, while $P(E_j|C_i)$ is calculated from the Monte Carlo simulation. In [30] it is shown that

smoothing the distribution of $P_n(C_i)$ before inserting in the next iteration step does not lead to better (smoother) results than without smoothing. Therefore the smoothing process is not applied in this analysis. The process converges and the iterations are stopped when the changes are smaller than the errors (which typically happens after about four iterations). The entries of the one-dimensional vectors $\vec{x}$ and $\vec{y}$ as well as the entries of the two-dimensional matrix $\mathcal{M}^{\mathrm{UFO}}$ carry the information on angle, momentum and particle type.

The Monte Carlo simulation of the HARP setup is based on GEANT4 [31]. The detector materials are accurately described in this simulation as well as the relevant features of the detector response and the digitization process. All relevant physics processes are considered, including multiple scattering, energy loss, absorption and re-interactions. The simulation is independent of the beam particle type because it only generates for each event exactly one secondary particle of a specific particle type inside the target material and propagates it through the complete detector. Owing to this fact the same simulation can be used for the three analyses of p-C, π^+-C and π^--C at 12 GeV/c. A small difference (at the few percent level) is observed between the efficiency calculated for events simulated with the single-particle Monte Carlo and with a simulation using a multi-particle hadron-production model. A similar difference is seen between the single-particle Monte Carlo and the efficiencies measured directly from the data. A momentum-dependent correction factor determined using the efficiency measured with the data is applied to take this into account. The track reconstruction used in this analysis and the simulation are identical to the ones used for the π^+ production in p-Be collisions [10]. A detailed description of the corrections and their magnitude can be found there.

The reconstruction efficiency (inside the geometrical acceptance) is larger than 95% above 1.5 GeV/c and drops to 80% at 0.5 GeV/c. The requirement of a match with a TOFW hit has an efficiency between 90% and 95% independent of momentum. The electron veto rejects about 1% of the pions and protons below 3 GeV/c with a remaining background of less than 0.5%. Below Cherenkov threshold the TOFW separates pions and protons with negligible background and an efficiency of $\approx$98% for pions. Above Cherenkov threshold the efficiency for pions is greater than 99% with only 1.5% of the protons mis-identified as a pion. The kaon background in the pion spectra is smaller than 1% and were subtracted assuming a similar angular and momentum distribution of kaons and pions.

The absorption and decay of particles is simulated by the Monte Carlo. The generated single particle can re-interact and produce background particles by hadronic or electromagnetic processes, thus giving rise to tracks in the dipole spectrometer. In such cases also the additional measurements are entered into the migration matrix thereby taking into account the combined effect of the generated particle and any secondaries it creates. The absorption correction is on average 20%, approximately independent of momentum. Uncertainties in the absorption of secondaries in the dipole spectrometer material are taken into account by a variation of 10% of this effect in the simulation. The effect of pion decay is treated in the same way as the absorption and is 20% at 500 MeV/c and negligible at 3 GeV/c.

The uncertainty in the production of background due to tertiary particles is larger. The average correction is $\approx$10% and up to 20% at 1 GeV/c. The correction includes reinteractions in the detector material as well as a small component coming from reinteractions in the target. The validity of the generators used in the simulation was checked by an analysis of HARP data with incoming protons, and charged pions on aluminium and carbon targets at lower momenta (3 GeV/c and 5 GeV/c). A 30% uncertainty of the secondary production was considered.

The unfolding matrix for the p-C analysis calculated this way is shown in Fig. 6 in the left upper panel. The very good separation in the three particle types (π^-, π^+ and proton) can be clearly seen. The angular (right upper panel) and momentum (lower panels) unfolding matrices have a nearly diagonal structure as expected. The binning chosen for these matrices is the same as the one used for the particle spectra (see section 3). The
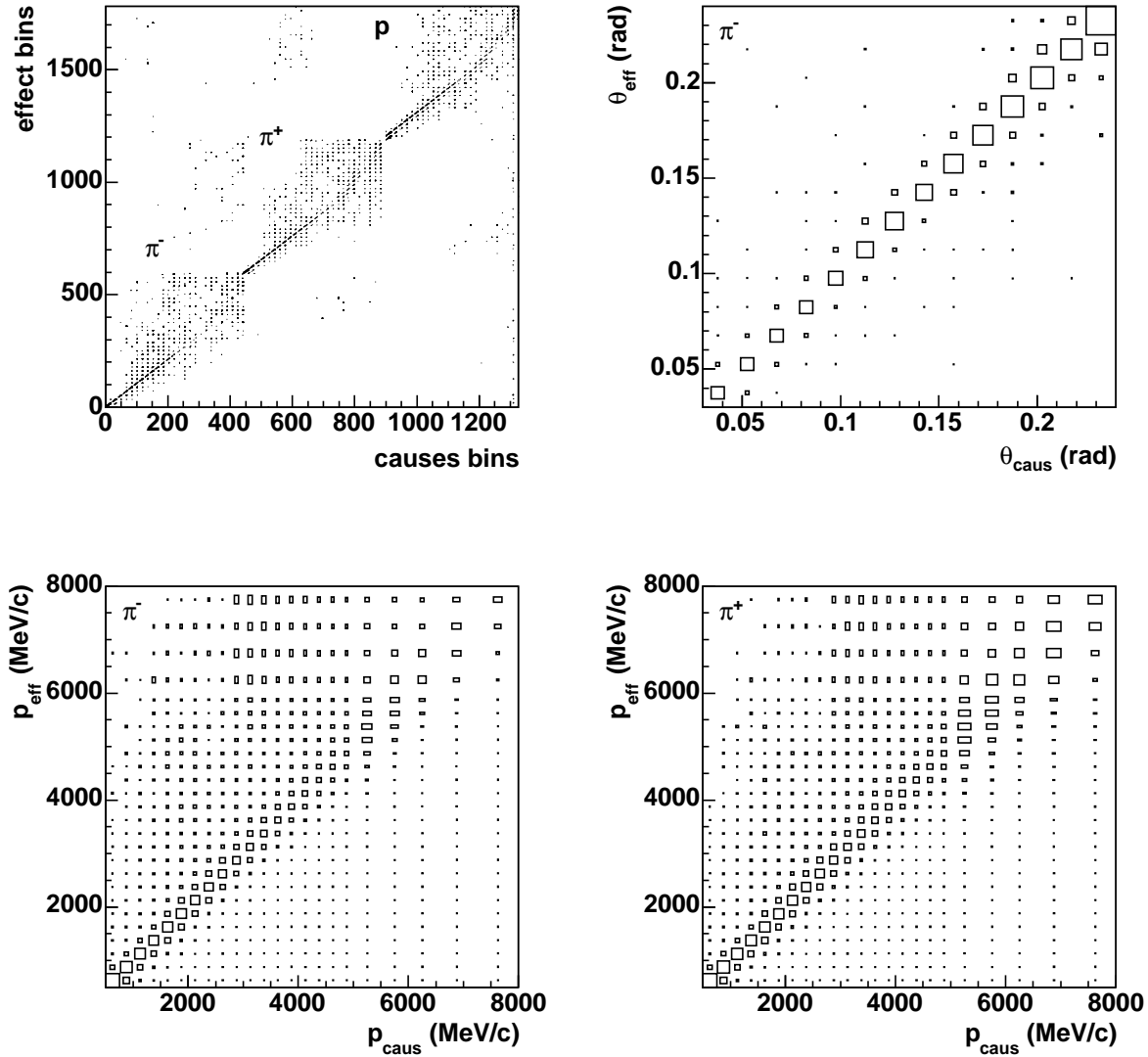
Figure 6: Graphical representation of migration matrices calculated for p-C analysis. The left upper panel shows the original migration matrix where the three dimensions (angle, momentum and particle type) are merged into one dimension as $n_{\theta,p,\alpha} = n_\theta + n_p \cdot n_\theta^{\max} + n_\alpha \cdot n_\theta^{\max} \cdot n_p^{\max}$, where $n_{\theta,p,\alpha}$ is the bin number in the final vectors and in the unfolding matrix; n_θ, n_p and n_α are the bin numbers in the three dimensions θ, p and α, respectively; $n_\theta^{\max}$ and $n_p^{\max}$ are the total number of bins in the observables p and α. The upper right panel shows an example of the angular migration matrix for π^- in one momentum causes-effects cell. The momentum migration matrices integrated over θ for π^- (left) and π^+ (right) are shown in the two lower panels.

unfolding matrices for the two other analyses (π^+-C and π^--C) are by construction very similar as the same Monte Carlo tracks are used, only the binning is different.

Owing to the large redundancy of the tracking system downstream of the target the detection efficiency is very robust under the usual variations of the detector performance during the long data taking periods. Since the momentum is reconstructed without making use of the upstream drift chamber (which is more sensitive in its performance to the beam intensity) the reconstruction efficiency is uniquely determined by the downstream system. No variation of the overall efficiency has been observed. The performance of the TOFW and CHE system have been monitored to be constant for the data taking periods used in this analysis. The calibration of the detectors was performed on a day-by-day basis.

2.5   Error estimation

The total statistical error of the corrected data is composed of the statistical error of the raw data, but also of the statistical error of the unfolding procedure, because the unfolding matrix is obtained from the data themselves and hence contributes also to the statistical error. The statistical error provided by the unfolding program is equivalent to the propagated statistical error of the raw data. In order to calculate the statistical error of the unfolding procedure a separate analysis following [30] is applied. It is briefly described below. The p-C dataset is divided into two independent data samples a and b, one sample contains all events with odd and the other all events with even event numbers. These data samples are unfolded in three different ways: 1) both samples are unfolded separately using the individually calculated unfolding matrix for each sample (set1); 2) each of the two samples are unfolded with the unfolding matrix calculated by using the whole dataset (set2); 3) the whole dataset is unfolded twice, using the unfolding matrices generated for each part of the split dataset (set3). For all three sets the same Monte Carlo input is applied. Since the statistics of the Monte Carlo sample is much larger compared to the statistics of the raw data, the statistical error related to the Monte Carlo is negligible. Set1 leads to the total statistical error of the unfolding result, set2 - to the statistical error of the raw data and set3 - to the statistical error of the unfolding matrix. For all sets the difference between the unfolded result of data sample a and b is calculated and divided by the propagated statistical error of the raw data a and b for each bin i in the effects space,

$$\Delta_{ab_i} = \frac{a_i - b_i}{\sqrt{\sigma_{a_i}^2 + \sigma_{b_i}^2}} \quad . \tag{6}$$

The distribution of Δ_{ab_i} shows for all three sets a Gaussian shape with a mean close to zero. The width of the distribution of Δ_{ab} for set1 is $k(\sigma_{\text{stat}}) = 2.0$, for set2 $k(\sigma_{\text{stat}}^{\text{data}}) = 0.98$ and for set3 $k(\sigma_{\text{stat}}^{\text{UFO}}) = 1.77$. A consistency check gives

$$k(\sigma_{\text{stat}}) = \sqrt{k^2(\sigma_{\text{stat}}^{\text{data}}) + k^2(\sigma_{\text{stat}}^{\text{UFO}})} \quad \longrightarrow \quad 2.0 \simeq \sqrt{0.98^2 + 1.77^2} \quad .$$

In conclusion, the statistical error provided by the unfolding procedure has to be multiplied globally by a factor of 2, which is done for the three analyses (p-C, π^+-C and π^--C) described here. This factor is somewhat dependent on the shape of the distributions. For example a value 1.7 was found for the analysis reported in Ref. [12].

The calculated statistical errors for each momentum–angle bin for all three datasets and separately for secondary π^- and π^+ are given in [33]. Due to the high statistics of the dataset, the momentum binning for the p-C dataset is chosen finer than for the other datasets. The limited statistics of the π^+-C data is reflected in a relatively large statistical error. Generally, the statistical error increases slightly with larger angle and significantly with

increasing momentum. The binning for the π^--C dataset is chosen to be the same as for the π^+-C data to make a direct comparison possible. The behaviour of statistical error as a function of momentum is shown in Fig. 7(left).

Different sources of systematic errors are considered in the analysis. Namely they are track yield corrections, particle identification, momentum and angular reconstruction. Following mainly [12], the strategy to calculate these systematic errors is to find different solutions of the unfolding problem, i.e. different 'causes' result vectors. The difference vector is used to create a covariance matrix for a specific systematic error. Three different methods are applied to calculate these different causes vectors: 1) variation of the normalization of the causes vector; 2) variation of the unfolding matrix; 3) variation of the raw data. The first method is used for the estimation of the systematic error of the track reconstruction efficiency. The uncertainties in the efficiency are estimated from the small differences observed between the data and the simulation.

The second method is applied for most of the systematic error estimations. The loss of secondary particles has to be considered due to particle decay and absorption in the detector materials as well as additional background particles generated in secondary reactions. These effects are simulated by Monte Carlo: two single-particle Monte Carlo simulations are generated, in the first simulation these effects are taken into account while not in the second one. Both Monte Carlo simulations are used for unfolding data, then the results are compared. The uncertainties in the absorption are estimated by a variation of 10% and the uncertainty in the production of background particle due to tertiary particles by a 30% variation [10]. The performance of particle identification, momentum and angular measurements are correlated due to the simultaneous unfolding process of these observables as described in section 2.4. The calculation of systematic errors of particle identification, angular and momentum resolution as well as of momentum scale is done by varying the acceptance criteria for these observables in the raw data and in the Monte Carlo. For the momentum resolution possible discrepancies up to 10% of the resolution are taken into account [10]. The systematic uncertainty in the momentum determination is estimated to be of the order of 2% using the elastic scattering analysis [10]. The angular scale was varied by 1%.

The third method is introduced for the estimation of the systematic error of the empty target subtraction. In addition to the standard empty target subtraction only 95% of the calculated empty target value is subtracted from the raw data[5]. The systematic error is taken from the difference of these two results. The statistical error of the empty target subtraction is taken into account as a diagonal statistical error in $N^{\alpha'}(p_i', \theta_j')$ by simple error propagation.

Due to the fact that kaons are not considered by the particle identification method in the current analysis [11] misidentified secondary kaons form an additional error source. To reduce this effect a specific Monte Carlo simulation only with secondary kaons is generated. Simulated kaons are classified as pions or protons according to the same PID criteria as applied to the data. The remaining mis-identified kaons are then subtracted assuming a 50% uncertainty on the K/π ratio. The central value of the K/π ratio was taken from Ref. [35]. This procedure also takes into account that decay muons from kaons produced in the target can be identified as pions in the spectrometer; these are subtracted by this procedure. We do not make an explicit correction for pions coming from decays of other particles created in the target. Pions created in strong decays are considered to be part of the inclusive production cross-sections. A small background coming from weak decays other than from charged kaons is neglected (such as K^0's and Λ^0's). These pions have a very small efficiency given the cuts applied in this analysis.

Following Ref. [12] the overall normalization of the results is calculated relative to the number of incident beam particles accepted by the selection. The uncertainty is 2% and 3% for incident protons and pions, respectively.

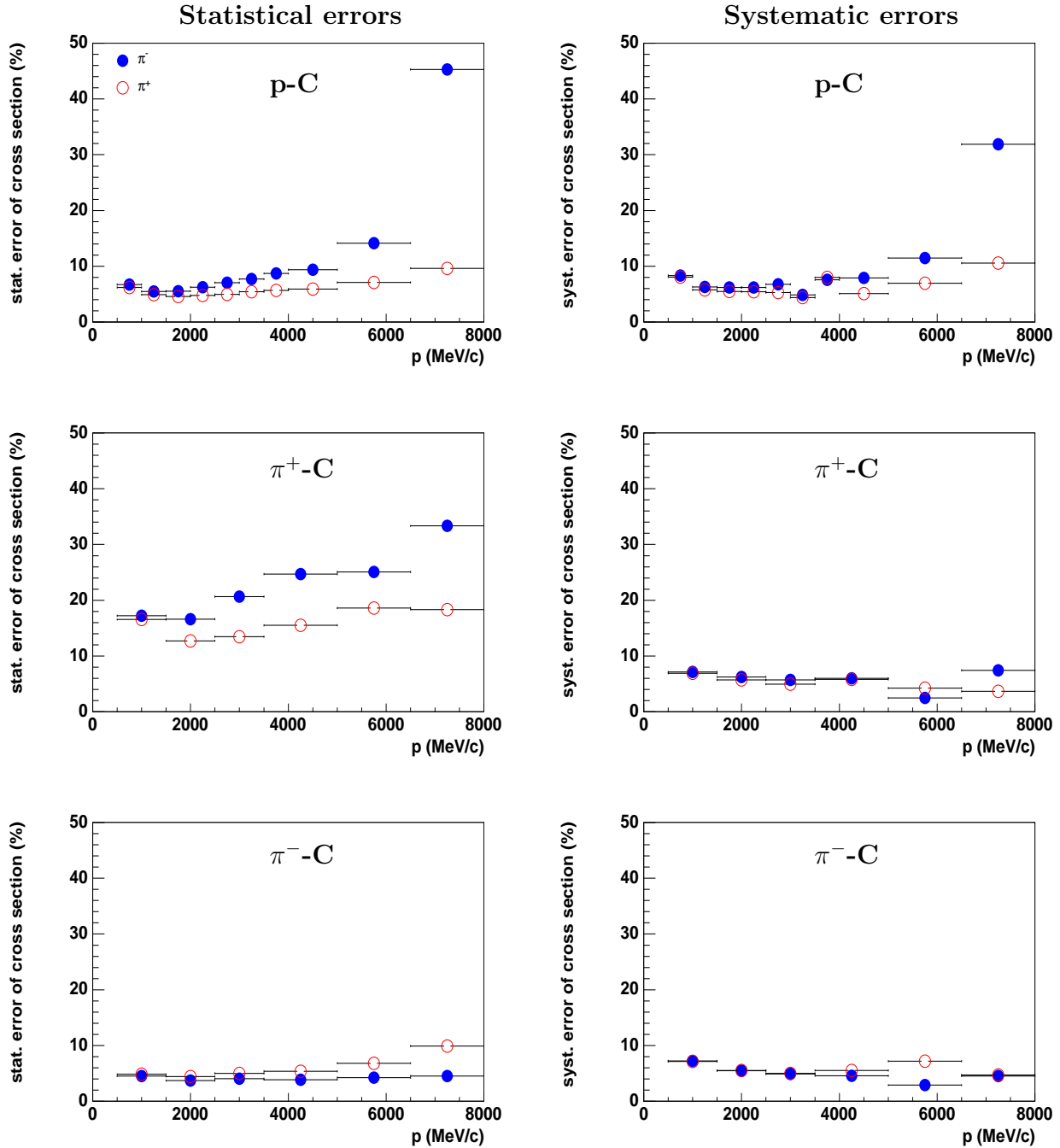[5]the maximum effect of the 5% λ_I target is to "absorb" 5% of the beam particles

Figure 7: Statistical (left) and total systematic (right) errors of π^-(filled circles) and π^+(open circles) as a function of momentum integrated over θ from 0.03 rad to 0.24 rad. Top: p-C, middle: π^+-C, bottom: π^--C.

As a result of these systematic error studies each error source can be represented by a covariance matrix. The sum of these matrices describes the total systematic error. Detailed information about the diagonal elements of the covariance matrix of the total systematic error for each momentum–angular bin can be found in [33]. In Fig. 7(right) the total systematic error integrated over angle is shown as a function of momentum. For the π^+-C and π^--C datasets the systematic error has a nearly flat distribution and is approximately 6%. For the p-C dataset the systematic error increases for higher momenta but also stays nearly constant around 8% below 6 GeV/c.

The dimensionless quantity δ_{diff}, expressing the typical error on the double-differential cross-section, is defined as follows

$$\delta_{\text{diff}} = \frac{\sum_i (\delta[d^2\sigma^\pi/(dpd\Omega)])_i}{\sum_i (d^2\sigma^\pi/(dpd\Omega))_i} \quad , \tag{7}$$

where i labels a given momentum–angular bin (p, θ), $(d^2\sigma^\pi/(dpd\Omega))_i$ is the central value for the double-differential cross-section measurement in that bin, and $(\delta[d^2\sigma^\pi/(dpd\Omega)])_i$ is the error associated with this measurement.

The dimensionless quantity δ_{int} is defined, expressing the fractional error on the integrated pion cross-section σ^π in the momentum range 0.5 GeV/c< p <8.0 GeV/c and the angular range 0.03 rad< θ <0.24 rad for the p-C data and in the angular range 0.03 rad< θ <0.21 rad for the $\pi^\pm$-C data[6], as follows

$$\delta_{\text{int}} = \frac{\sqrt{\sum_{i,j} (\Delta p \Delta\Omega)_i C_{ij} (\Delta p \Delta\Omega)_j}}{\sum_i (d^2\sigma^\pi/dpd\Omega)_i (\Delta p \Delta\Omega)_i} \quad , \tag{8}$$

where $(d^2\sigma^\pi/dpd\Omega)_i$ is the double-differential cross-section in bin i, $(\Delta p \Delta\Omega)_i$ is the corresponding phase space element, and C_{ij} is the covariance matrix of the double-differential cross-section. Then $\sqrt{C_{ii}}$ corresponds to the error $(\delta[d^2\sigma^\pi/(dpd\Omega)])_i$ in Eq. (7).

The values of δ_{diff} and δ_{int} are summarized for all specific systematic error sources in Table 3 for p-C data, in Table 4 for π^+-C data and in Table 5 for π^--C data. The systematic errors are of the same order for all three datasets, δ_{diff} = 9%-11% and δ_{int} = 5%-8%. The dominant error sources are given by particle absorption and the subtraction of tertiary particles. The decay correction is technically made as part of the absorption correction and reported under "absorption". The errors of momentum and angular reconstruction are less important and the errors caused by the particle misidentification are negligible. For the datasets with positively charged beam the systematic error is smaller for π^+ and for π^--C dataset it is smaller for π^-.

Systematic and statistical errors are of the same order for the p-C and the π^--C data. For the π^+-C dataset the statistical error is dominating the total error. The π^--C data have the smallest total error due to the data statistics and chosen bin width.

There is a certain amount of correlation between the systematic errors in the different spectra. In the comparison of production spectra of the same secondary particle type by different incoming particles, the absorption and decay errors cancel. One also expects the tertiary subtraction uncertainty to cancel partially, although this depends on the details of the production models. (For example, the uncertainty in the background in the π^+ spectra measured in the π^+ beam is expected to be correlated to the background for π^- in the π^- beam, but less so for opposite charges.) Of the other relatively important errors the systematic component of the empty target subtraction and the momentum scale error cancel between the datasets. The overall normalization errors are largely independent.

---

[6]The binning of the $\pi^\pm$ data was chosen to accommodate the lower statistics of the π^+ data and is only determined for θ <0.21 rad.

Table 3: Summary of the uncertainties affecting the double-differential and integrated cross-section measurements of p-C data.

Error category	Error source	$\delta^{\pi^-}_{\text{diff}}(\%)$	$\delta^{\pi^-}_{\text{int}}(\%)$	$\delta^{\pi^+}_{\text{diff}}(\%)$	$\delta^{\pi^+}_{\text{int}}(\%)$
Statistical	Data statistics	12.8	3.2	10.8	2.5
Track yield corrections	Reconstruction efficiency	1.6	1.3	1.1	0.5
	Pion, proton absorption	4.2	3.7	3.7	3.2
	Tertiary subtraction	9.8	4.2	8.6	3.7
	Empty target subtraction	1.2	1.2	1.2	1.2
	Subtotal	10.8	5.9	9.5	5.1
Particle identification	Electron veto	< 0.1	< 0.1	< 0.1	< 0.1
	Pion, proton ID correction	< 0.1	0.1	0.1	0.1
	Kaon subtraction	< 0.1	< 0.1	< 0.1	< 0.1
	Subtotal	0.1	0.1	0.1	0.1
Momentum reconstruction	Momentum scale	2.6	0.4	2.8	0.3
	Momentum resolution	0.7	0.2	0.8	0.3
	Subtotal	2.7	0.5	2.9	0.4
Angle reconstruction	Angular scale	0.5	0.1	1.3	0.5
Systematic error	Subtotal	11.2	5.9	10.0	5.1
Overall normalization	Subtotal	2.0	2.0	2.0	2.0
All	Total	17.1	7.0	14.9	6.1

Table 4: Summary of the uncertainties affecting the double-differential and integrated cross-section measurements of π^+-C data.

Error category	Error source	$\delta^{\pi^-}_{\text{diff}}(\%)$	$\delta^{\pi^-}_{\text{int}}(\%)$	$\delta^{\pi^+}_{\text{diff}}(\%)$	$\delta^{\pi^+}_{\text{int}}(\%)$
Statistical	Data statistics	41.8	6.4	34.5	7.2
Track yield corrections	Reconstruction efficiency	1.4	0.7	0.9	0.5
	Pion, proton absorption	4.0	2.1	3.3	2.7
	Tertiary subtraction	9.3	4.7	7.6	6.3
	Empty target subtraction	1.0	0.7	1.0	1.0
	Subtotal	10.3	5.2	8.4	6.9
Particle identification	Electron veto	< 0.1	< 0.1	< 0.1	< 0.1
	Pion, proton ID correction	0.1	< 0.1	0.2	0.2
	Kaon subtraction	< 0.1	< 0.1	< 0.1	< 0.1
	Subtotal	0.1	0.1	0.2	0.2
Momentum reconstruction	Momentum scale	3.2	0.2	3.6	0.5
	Momentum resolution	0.9	0.2	1.1	0.3
	Subtotal	3.3	0.3	3.8	0.6
Angle reconstruction	Angular scale	1.7	0.1	1.3	0.5
Systematic error	Subtotal	10.9	5.3	9.2	7.0
Overall normalization	Subtotal	3.0	3.0	3.0	3.0
All	Total	43.7	8.5	35.8	10.2

Table 5: Summary of the uncertainties affecting the double-differential and integrated cross-section measurements of π^--C data.

Error category	Error source	$\delta^{\pi^-}_{\mathrm{diff}}(\%)$	$\delta^{\pi^-}_{\mathrm{int}}(\%)$	$\delta^{\pi^+}_{\mathrm{diff}}(\%)$	$\delta^{\pi^+}_{\mathrm{int}}(\%)$
Statistical	Data statistics	8.5	2.2	10.0	1.9
Track yield corrections	Reconstruction efficiency	1.3	1.1	0.7	0.4
	Pion, proton absorption	3.5	3.1	3.8	2.3
	Tertiary subtraction	7.9	6.8	9.0	5.3
	Empty target subtraction	0.9	0.8	0.9	0.6
	Subtotal	8.8	7.6	9.8	5.8
Particle identification	Electron veto	< 0.1	< 0.1	< 0.1	< 0.1
	Pion, proton ID correction	0.1	0.1	0.1	0.1
	Kaon subtraction	< 0.1	< 0.1	< 0.1	< 0.1
	Subtotal	0.1	0.1	0.1	0.1
Momentum reconstruction	Momentum scale	2.3	0.7	2.7	0.3
	Momentum resolution	0.6	0.2	0.5	0.2
	Subtotal	2.4	0.7	2.7	0.4
Angle reconstruction	Angular scale	0.6	0.3	0.7	< 0.1
Systematic error	Subtotal	9.1	7.6	10.2	5.8
Overall normalization	Subtotal	3.0	3.0	3.0	3.0
All	Total	12.6	8.2	14.4	6.5

3 Results

The results of the measurements of the double-differential cross-sections for positive and negative pions in p-C, π^+-C and π^--C interactions at 12 GeV/c in the laboratory system are presented as a function of momentum for various angular bins in Figs. 8, 9 and 10, respectively. The central values and square-root of the diagonal elements of the covariance matrix are listed in Tables 10-12 in Appendix A. The kinematic range of the measurements covers the momentum region from 0.5 GeV/c to 8.0 GeV/c and the angular range from 0.03 rad to 0.24 rad for p-C and from 0.03 rad to 0.21 rad for π^+-C and π^--C data. The error bars correspond to the combined statistical and systematic errors as described in section 2.5. The overall normalization error of 2% and 3% for the normalization of incident protons and pions, respectively, is not shown.

The shapes of the production cross-sections are similar for secondary π^+ and π^- as well as for different datasets. For larger angles the spectra are softer and show a leading particle effect for produced π^+ in p-C and π^+-C reactions and for π^- in π^--C reactions. The distribution of secondary π^+ in π^+-C reactions show a very similar behaviour as the distribution of secondary π^- in π^--C reactions as expected because of the isospin symmetry of $\pi^+ + C \to \pi^+ + X$ and $\pi^- + C \to \pi^- + X$ reactions. The corresponding behaviour can be seen for π^- in π^+-C interactions and for π^+ in π^--C interactions. The π^+/π^- ratio is larger than unity in the positive particle beams and smaller than unity in the π^- beam.

In section 3.1 the measured cross-sections are fitted to a Sanford-Wang parametrization while in section 3.2 a comparison of HARP p-C data with predictions of different hadronic interaction models is shown.
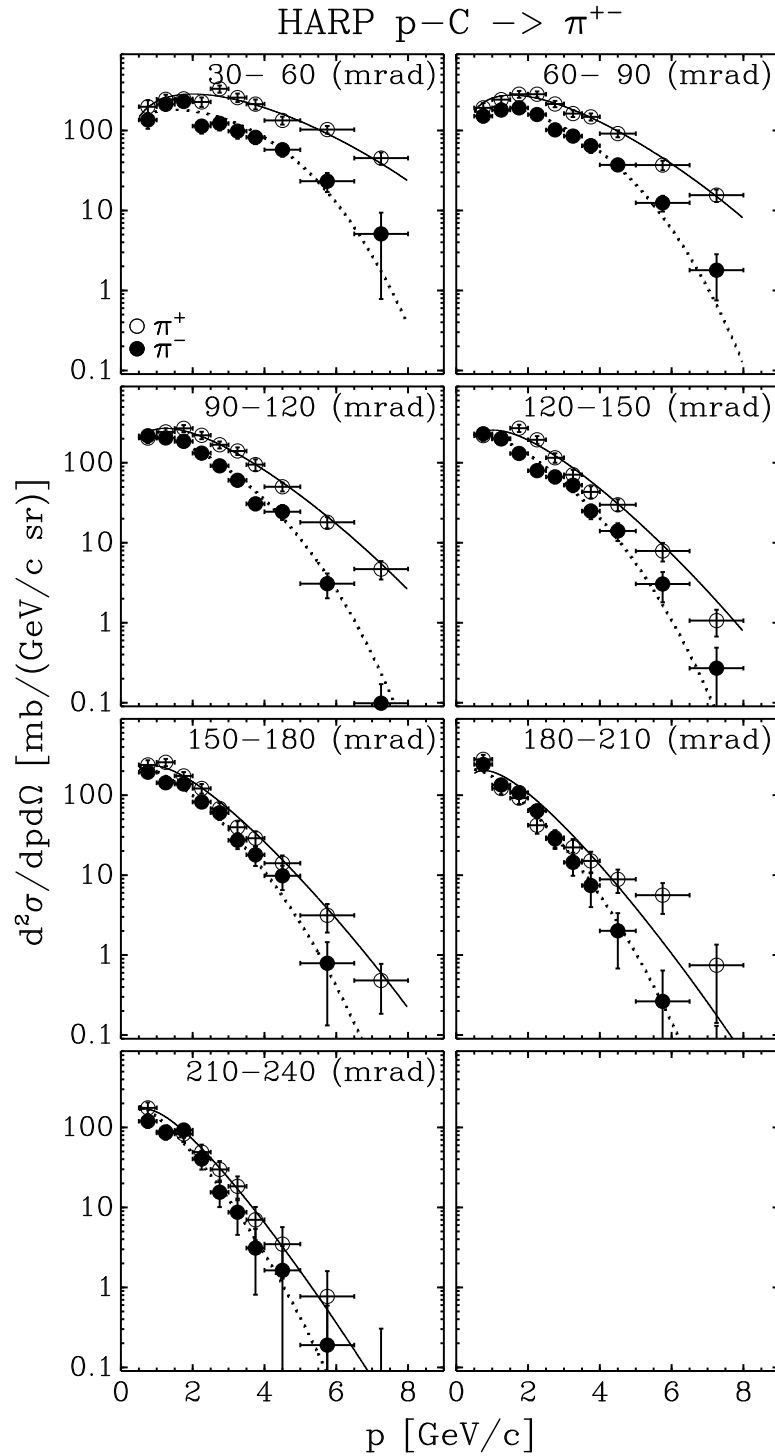
Figure 8: Measurement of the double-differential production cross-section of positive (open circles) and negative (filled circles) pions from 12 GeV/c protons on carbon as a function of pion momentum, p, in bins of pion angle, θ, in the laboratory frame. Seven panels show different angular bins from 30 mrad to 240 mrad (the corresponding angular interval is printed on each panel). The error bars shown include statistical errors and all (diagonal) systematic errors. The curves show the Sanford-Wang parametrization of Eq. 9 with parameter values given in Table 6.
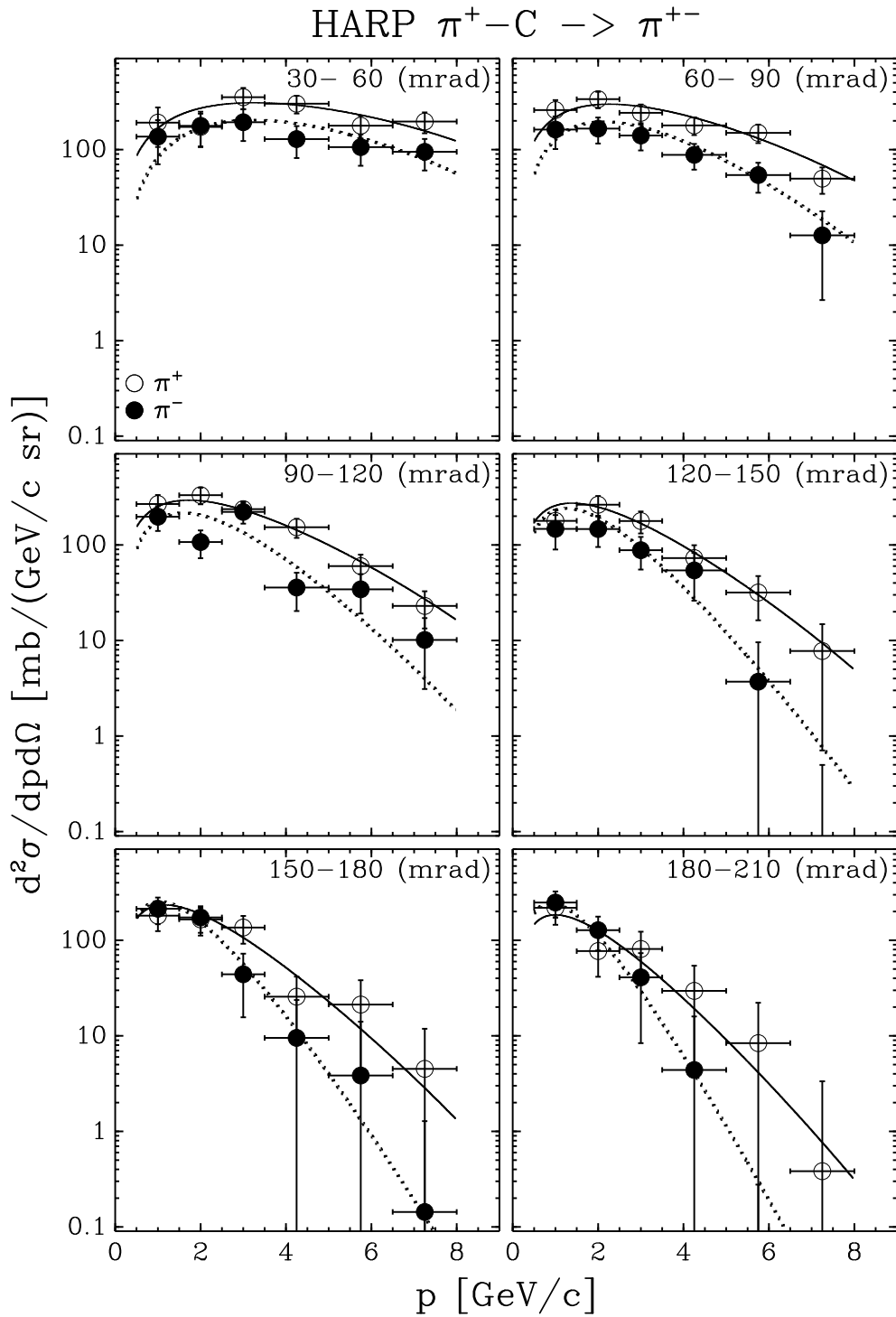
Figure 9: Measurement of the double-differential production cross-section of positive (open circles) and negative (filled circles) pions from 12 GeV/c π^+ on carbon as a function of pion momentum, p, in bins of pion angle, θ, in the laboratory frame. Six panels show different angular bins from 30 mrad to 210 mrad (the corresponding angular interval is printed on each panel). The error bars shown include statistical errors and all (diagonal) systematic errors. The curves show the Sanford-Wang parametrization of Eq. 9 with parameter values given in Table 8.
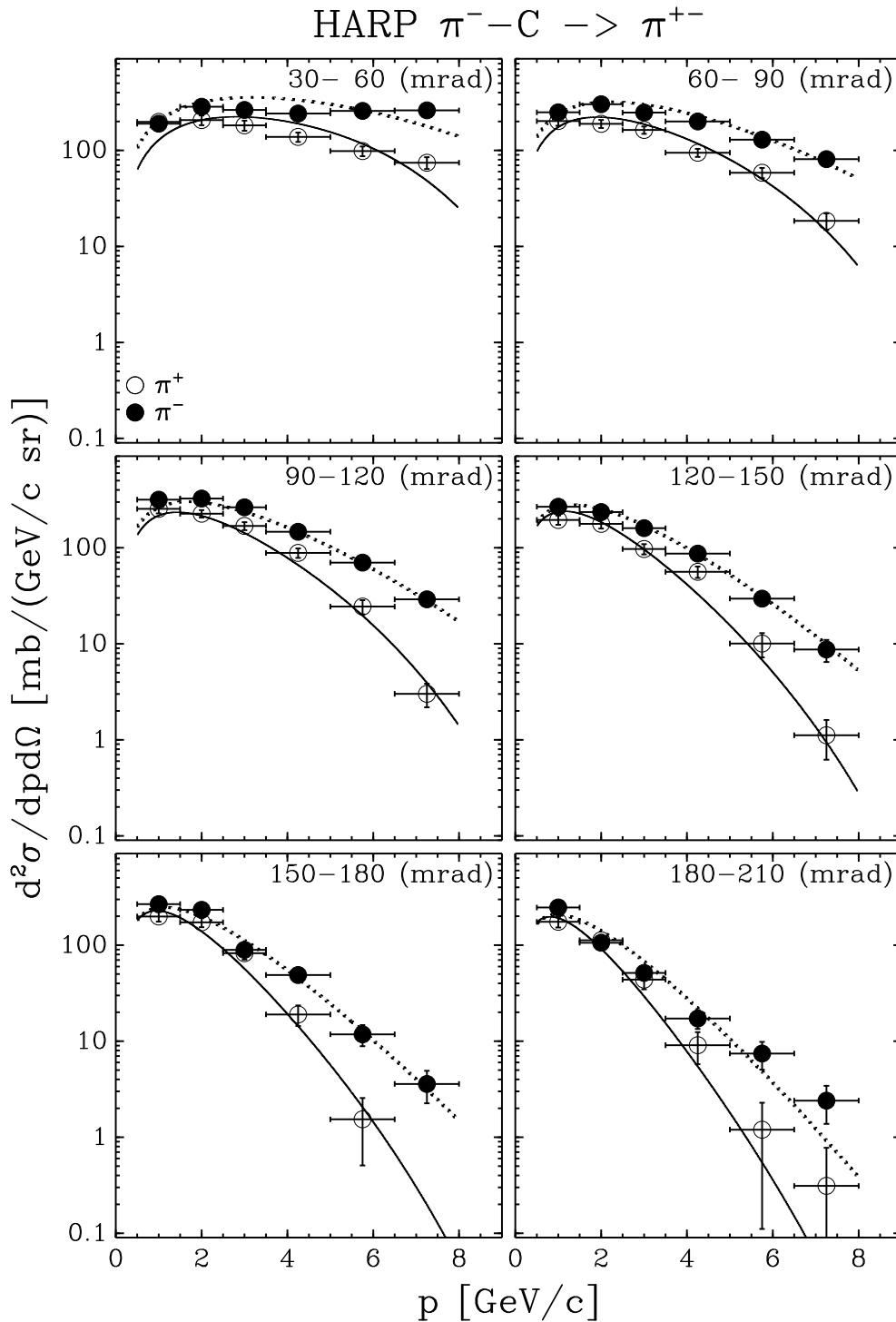
Figure 10: Measurement of the double-differential production cross-section of positive (open circles) and negative (filled circles) pions from 12 GeV/c π^- on carbon as a function of pion momentum, p, in bins of pion angle, θ, in the laboratory frame. Six panels show different angular bins from 30 mrad to 210 mrad (the corresponding angular interval is printed on each panel). The error bars shown include statistical errors and all (diagonal) systematic errors. The curves show the Sanford-Wang parametrization of Eq. 9 with parameter values given in Table 8.

Table 6: Sanford-Wang parameters and errors obtained by fitting the p–C dataset.

Param	p–C	
	π^-	π^+
c_1	144.46 ± 65.593	214.92 ± 93.307
c_2	0.60749 ± 0.34902	0.95748 ± 0.44512
c_3	16.947 ± 10.876	3.0906 ± 1.2601
$c_4 = c_5$	3.2512 ± 1.3657	1.6876 ± 1.5230
c_6	5.9304 ± 1.2561	5.5728 ± 0.71771
c_7	0.17152 ± 0.074772	0.15597 ± 0.06683
c_8	27.241 ± 12.232	30.873 ± 13.388
χ^2/NDF	$95.6/63$	$147.7/63$

3.1 Sanford-Wang parametrization

Sanford and Wang [37] have developed an empirical parametrization for describing the production cross-sections of mesons in proton-nucleus interactions. This parametrization has the functional form:

$$\frac{d^2\sigma^\pi}{dpd\Omega}(p,\theta) = c_1 p^{c_2}\left(1 - \frac{p}{p_{\mathrm{beam}}}\right)\exp\left[-c_3\frac{p^{c_4}}{p_{\mathrm{beam}}^{c_5}} - c_6\theta\left(p - c_7 p_{\mathrm{beam}}\cos^{c_8}\theta\right)\right] \quad , \tag{9}$$

where

- $\frac{d^2\sigma^\pi}{dpd\Omega}(p,\theta)$ is the cross-section in mb/(GeV/c sr) for secondary pions as a function of momentum p (in GeV/c) and angle θ (in radians) of the secondary particles;

- p_{beam} is the beam momentum in GeV/c;

- $c_1, ..., c_8$ are free parameters obtained from fits to meson production data.

The parameter c_1 is an overall normalization factor, the four parameters c_2, c_3, c_4, c_5 can be interpreted as describing the momentum distribution of the secondary pions in the forward direction, and the three parameters c_6, c_7, c_8 as describing the angular distribution for fixed secondary and beam momenta, p and p_{beam}.

This empirical formula has been fitted to the measured π^+ and π^- production spectra in p–C, π^+–C and π^-–C reactions at 12 GeV/c reported here. As initial values for these fits the parameters of the Sanford-Wang fit of the p–Al HARP analysis at 12.9 GeV/c are taken from [9]. The original Sanford-Wang parametrization has been proposed to describe incoming proton data. We apply the same parametrization also to the π^+–C and π^-–C datasets.

In the χ^2 minimization procedure the full error matrix is used. For these fits the Sanford-Wang parametrization has been integrated over momentum and angular bin widths of the data. However, the results are nearly identical to the fit results without integration over individual bins. Concerning the parameters estimation, the best-fit values of the Sanford-Wang parameter set discussed above are reported in Tables 6 and 8, together with their errors. Since for some fits the c_3 parameter tends to zero, we decided to fix this parameter and to set it to zero. For these fits the c_4 and c_5 parameters are irrelevant (see Eq. 9). The correlation coefficients among the Sanford-Wang parameters are shown in Tables 7 and 9. The fit parameter errors are estimated by requiring $\Delta\chi^2 \equiv \chi^2 - \chi^2_{\mathrm{min}} = 8.18$ (5.89), corresponding to the 68.27% confidence level region for seven (five) variable parameters. Some parameters are strongly correlated resulting in large errors of the extracted parameters.

Table 7: Correlation coefficients among the Sanford-Wang parameters, obtained by fitting the p–C dataset.

				π^-			
Parameter	c_1	c_2	c_3	$c_4 = c_5$	c_6	c_7	c_8
c_1	1.000						
c_2	-0.433	1.000					
c_3	-0.041	-0.548	1.000				
$c_4 = c_5$	-0.113	-0.535	0.950	1.000			
c_6	-0.535	0.622	-0.035	0.127	1.000		
c_7	-0.837	0.121	0.024	0.050	0.214	1.000	
c_8	-0.206	-0.316	0.028	-0.025	-0.360	0.611	1.000
				π^+			
Parameter	c_1	c_2	c_3	$c_4 = c_5$	c_6	c_7	c_8
c_1	1.000						
c_2	0.151	1.000					
c_3	0.061	-0.151	1.000				
$c_4 = c_5$	-0.461	-0.860	0.351	1.000			
c_6	-0.544	0.248	-0.373	0.065	1.000		
c_7	-0.790	-0.004	-0.168	0.115	0.333	1.000	
c_8	-0.083	-0.275	0.092	0.080	-0.416	0.488	1.000

The measurements for π^- and π^+ in p–C, π^+–C and π^-–C reactions are compared to the Sanford-Wang parametrizations in Figs. 8, 9 and 10, respectively. One notes that the Sanford-Wang parametrization is not able to describe some of the data spectral features especially at low and high momenta. The goodness-of-fit of the Sanford-Wang parametrization hypothesis can be assessed by considering χ^2 per number of degrees of freedom (NDF) given in Tables 6 and 8. Especially for the π^- data one finds a high value of χ^2. This may not be surprising since the parametrization was developed for pion production by incoming protons rather than by incoming pions. The π^- data with their high statistics are more likely to reveal discrepancies than the π^+ data which have much lower statistical significance.

For tuning and modifying models, often a parametrization of data like the Sanford-Wang formula is used. This can be a suitable method to interpolate between measured energy and phase space regions. However, this method has some shortcomings. By construction, the reliability of parametrizations for extrapolating to energy

Table 8: Sanford-Wang parameters and errors obtained by fitting the π^+–C and π^-–C datasets.

	π^+–C		π^-–C	
Param	π^-	π^+	π^-	π^+
c_1	41.448 ± 45.572	109.24± 114.73	156.49 ± 56.132	78.963 ± 34.332
c_2	1.8316 ± 0.61113	1.2130 ± 0.57892	1.1673 ± 0.17019	1.3561 ± 0.21690
c_3	0. (fixed)	0. (fixed)	0. (fixed)	7.1493 ± 28.024
$c_4=c_5$	—	—	—	5.1098 ± 7.2508
c_6	10.074 ± 1.8426	5.7823 ± 1.9875	5.6525 ± 0.54217	8.0965 ± 0.73121
c_7	0.22877 ± 0.098638	0.25667 ± 0.17396	0.19908 ± 0.06052	0.21960 ± 0.055566
c_8	18.056 ± 15.934	36.139 ± 25.437	30.368 ± 9.9403	25.561 ± 9.1022
χ^2/NDF	37.4/31	18.5/31	133.6/31	136.7/29

and phase space regions where no data are available is limited (see [33] for a more detailed discussion).

Detailed inspection of Figs. 8, 9 and 10 allows us to conclude that at high momenta and in particular at large angles the parametrization does not describe the data well enough. Especially for π^+ momentum spectra at angles larger than 0.18 rad, the Sanford-Wang fit deviates considerably from the data and it should not be used in the angular range above 0.18 rad.

3.2   Comparison of p–C HARP data at 12 GeV/c with model predictions

A comparison of π^- and π^+ production in p–C reactions at 12 GeV/c with different model predictions is shown in Figs. 11 and 12. The three hadronic interaction models used for this comparison are GHEISHA [38], UrQMD [39] and DPMJET-III [40]. These are the models typically used in air shower simulations. The GHEISHA and UrQMD are implemented in CORSIKA [36] as low energy models (below 80 GeV), whereas the DPMJET-III is mostly used at higher energies but it is also able to make predictions at lower energies. Comparing the predictions of these models to the measured data, distinct discrepancies at low and high momenta become visible. Especially the decrease of the cross-section at very low momenta is not well described by the models. For π^+, the prediction of the DPMJET-III seems relatively good, however, this model underestimates the π^- production at low momenta. At large momenta the predictions of the three models are similar to each other, but none of them provides an acceptable description of the data.

We have also compared our measurements with predictions of GEANT4 [31] models relevant in the energy domain studied here (FTFP [41], QGSP [41, 42] and LHEP [31, 43]). The corresponding plots are presented in Figs. 13 and 14 (for incoming protons), in Figs. 15 and 16 (for incoming π^+) and in Figs. 17 and 18 (for incoming π^-). From these plots one can conclude that the predictions of FTFP and QGSP models are closer to the HARP data compared to the LHEP model. For the π^- and π^+ data the DPMJET-III model is shown in the same figure. The predictions of the latter model are very close to those of the FTFP model.

We have made a χ^2 comparison between the HARP data and all the models shown here. The full HARP error matrix has been used, and MC statistical errors (small but non-negligible) have been also taken into account. The conclusions of this study are given below. None of the models describe our data accurately. However, in general these models tend to describe the π^+ production more correctly than π^- production for all three incoming particle types. Different models are preferable, depending on projectile type and on the charge of the pion produced. In particular,

- for proton projectiles and π^+ production, UrQMD, FTFP and GHEISHA give the best results;

- for proton projectiles and π^- production, FTFP is preferable;

- for π^+ projectiles and π^+ production and for π^- projectiles and π^- production, DPMJET-III is best;

- for π^+ projectiles and π^- production and for π^- projectiles and π^+ production, QGSP describes the data best.

4   Summary and conclusions

The results reported in this article contribute to the precise calculations of atmospheric neutrino fluxes and to the improvement of our understanding of extended air shower simulations and hadronic interactions at low energies.

Figure 11: Comparison of the measured double-differential production cross-section of π^- in p–C reactions at 12 GeV/c (points with error bars) with GHEISHA, UrQMD and DPMJET-III model predictions. Seven panels show different angular bins from 30 mrad to 240 mrad (the corresponding angular interval is printed on each panel).

Figure 12: Comparison of the measured double-differential production cross-section of π^+ in p–C reactions at 12 GeV/c (points with error bars) with GHEISHA, UrQMD and DPMJET-III model predictions. Seven panels show different angular bins from 30 mrad to 240 mrad (the corresponding angular interval is printed on each panel).
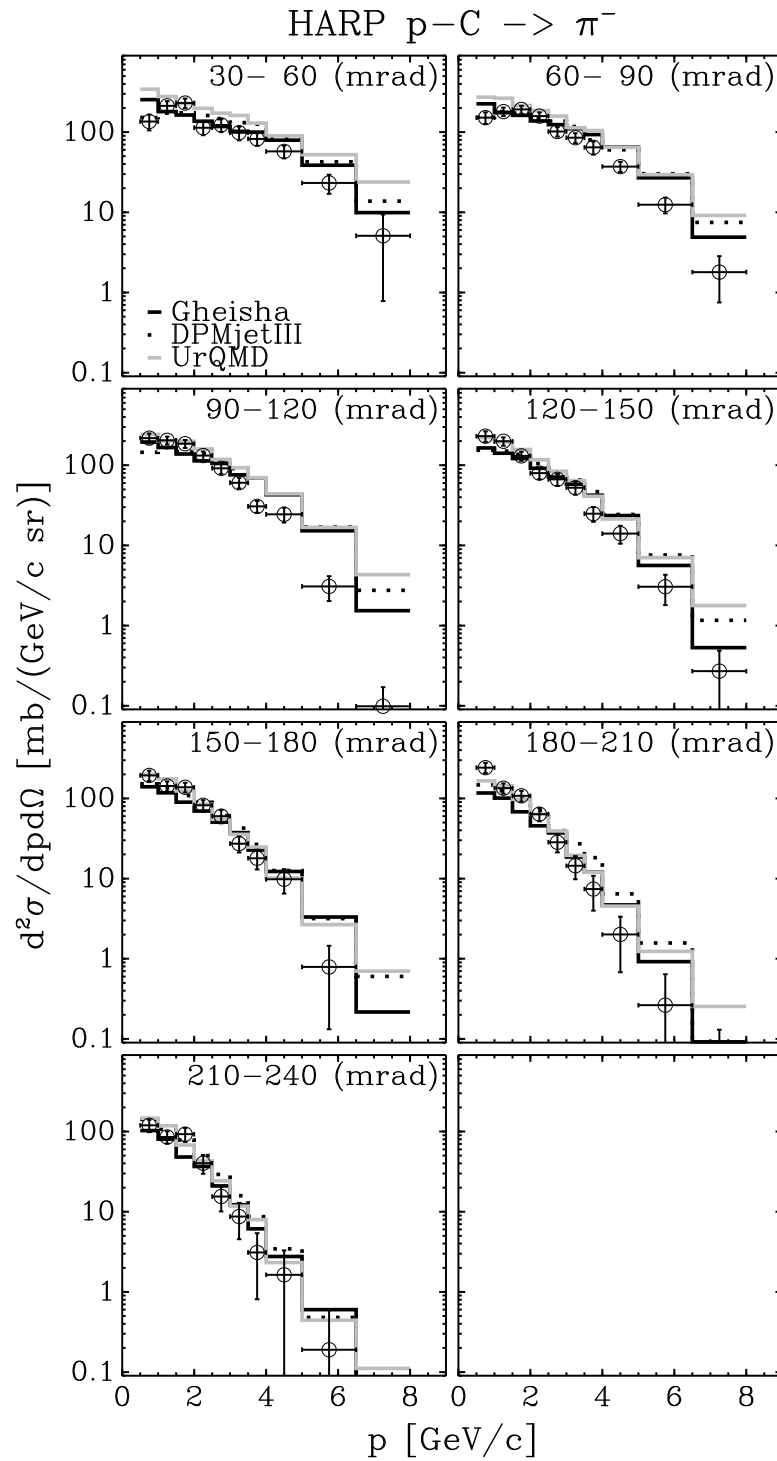
Figure 13: Comparison of the measured double-differential production cross-section of π^- in p–C reactions at 12 GeV/c (points with error bars) with predictions of relevant GEANT4 models. Seven panels show different angular bins from 30 mrad to 240 mrad (the corresponding angular interval is printed on each panel).

Figure 14: Comparison of the measured double-differential production cross-section of π^+ in p–C reactions at 12 GeV/c (points with error bars) with predictions of relevant GEANT4 models. Seven panels show different angular bins from 30 mrad to 240 mrad (the corresponding angular interval is printed on each panel).
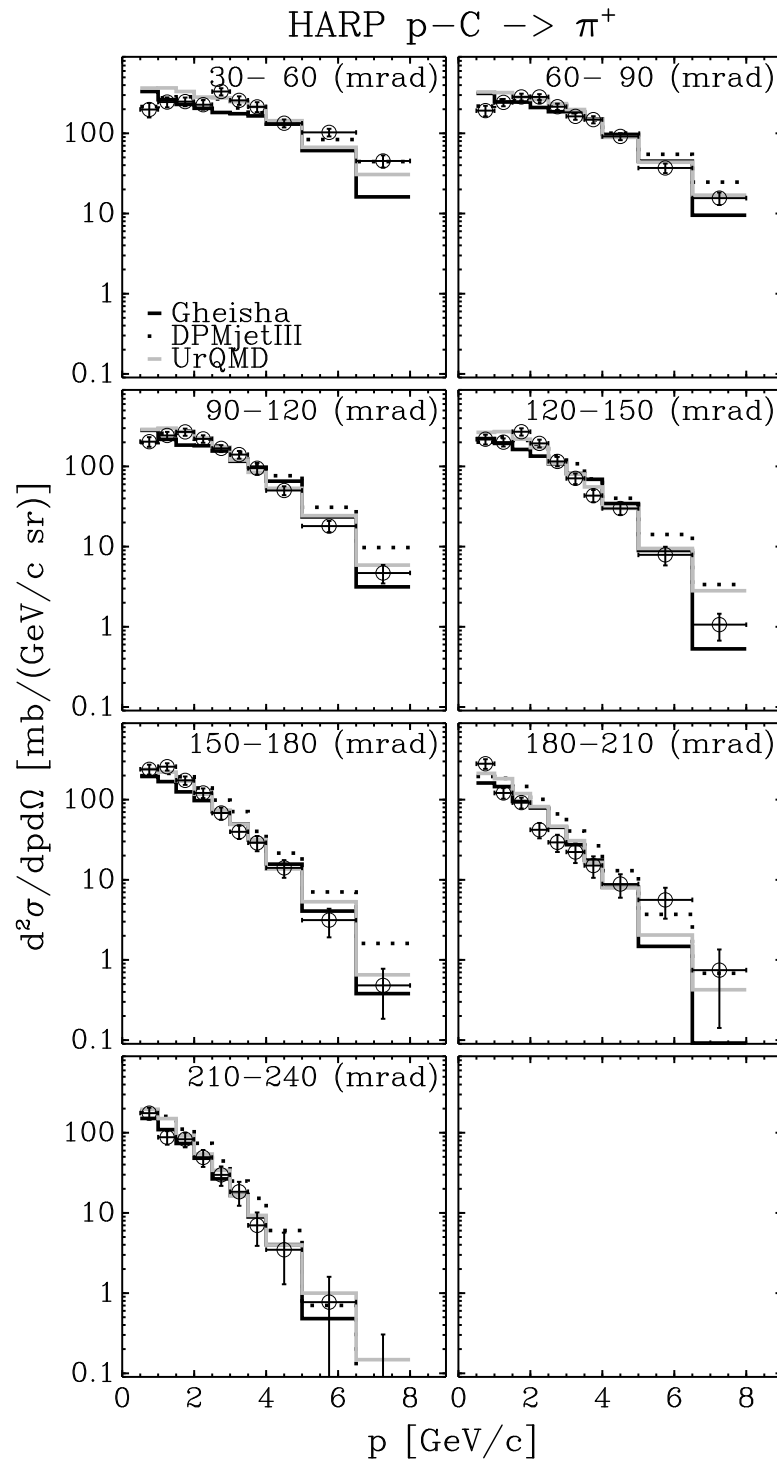
Figure 15: Comparison of the measured double-differential production cross-section of π^- in π^+–C reactions at 12 GeV/c (points with error bars) with predictions of relevant GEANT4 and DPMJET-III models. Six panels show different angular bins from 30 mrad to 210 mrad (the corresponding angular interval is printed on each panel).
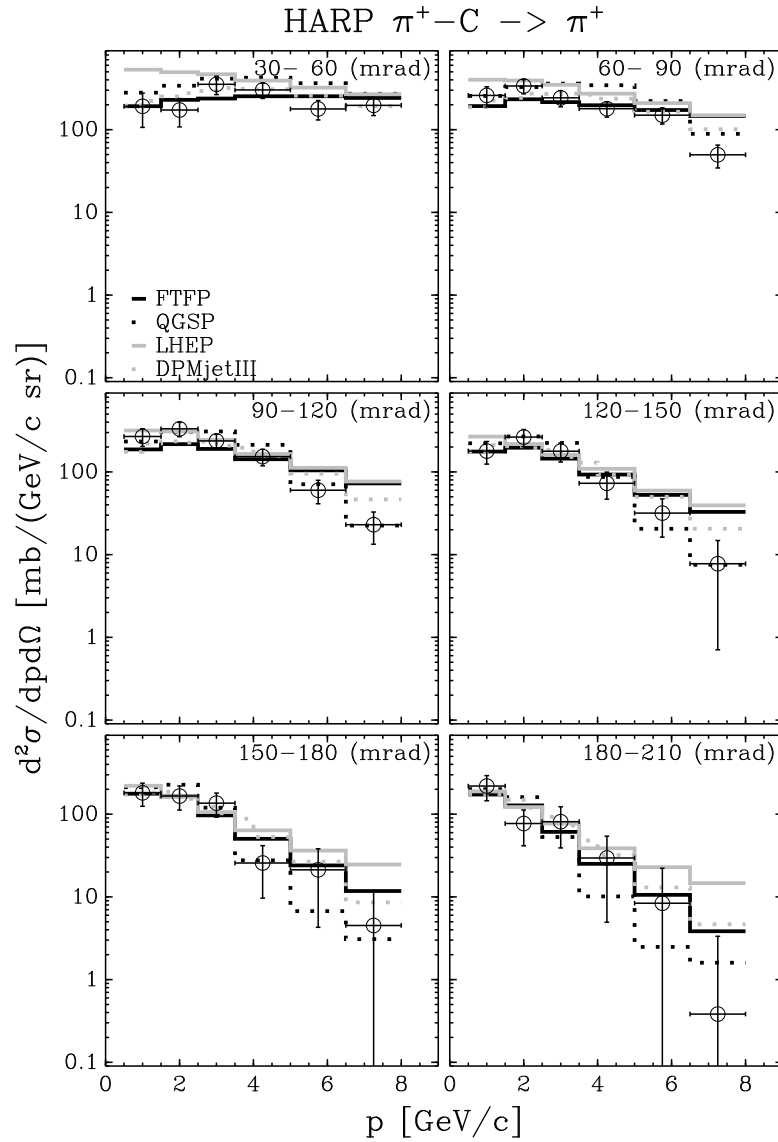
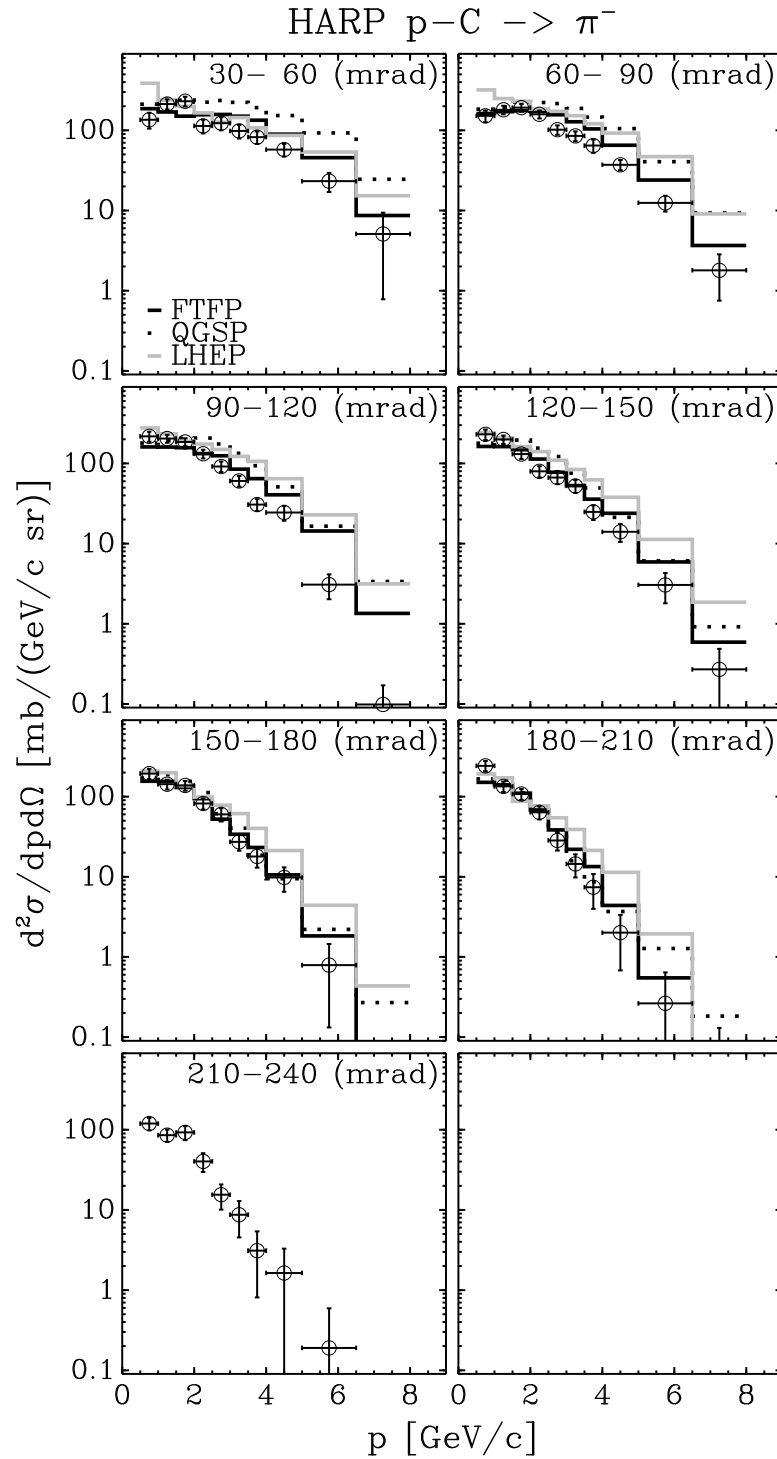Figure 16: Comparison of the measured double-differential production cross-section of π^+ in π^+–C reactions at 12 GeV/c (points with error bars) with predictions of relevant GEANT4 and DPMJET-III models. Six panels show different angular bins from 30 mrad to 210 mrad (the corresponding angular interval is printed on each panel).
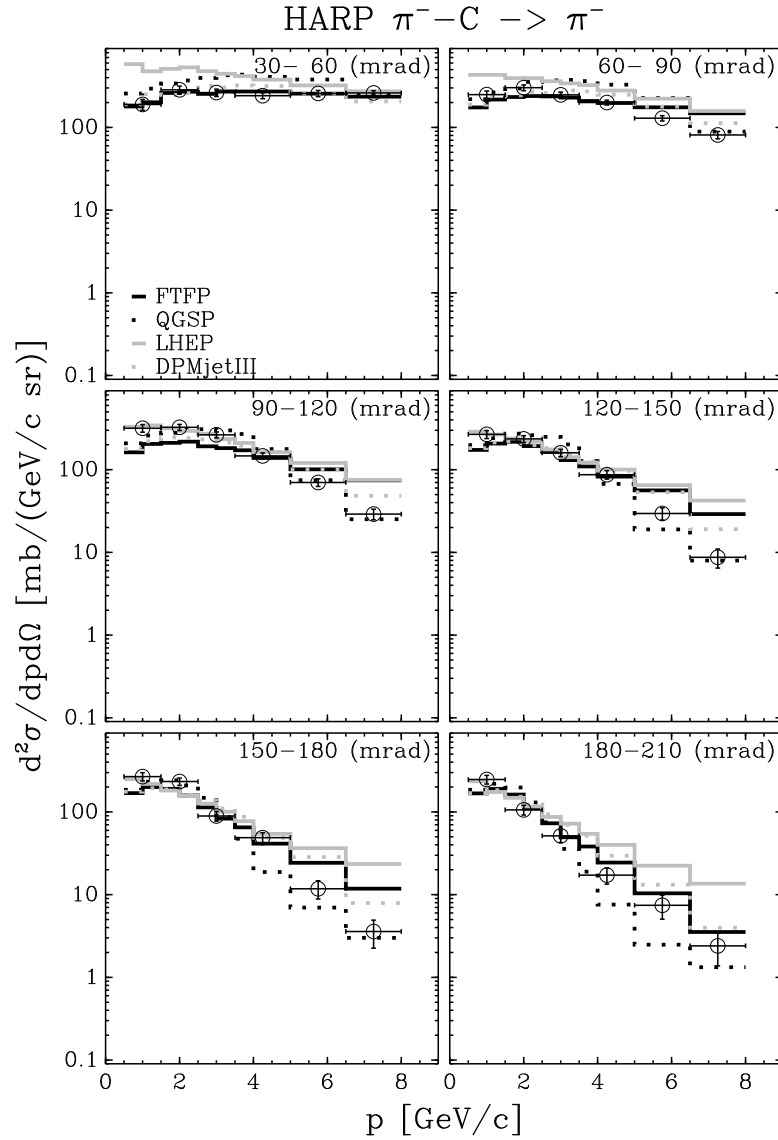
Figure 17: Comparison of the measured double-differential production cross-section of π^- in π^-–C reactions at 12 GeV/c (points with error bars) with predictions of relevant GEANT4 and DPMJET-III models. Six panels show different angular bins from 30 mrad to 210 mrad (the corresponding angular interval is printed on each panel).
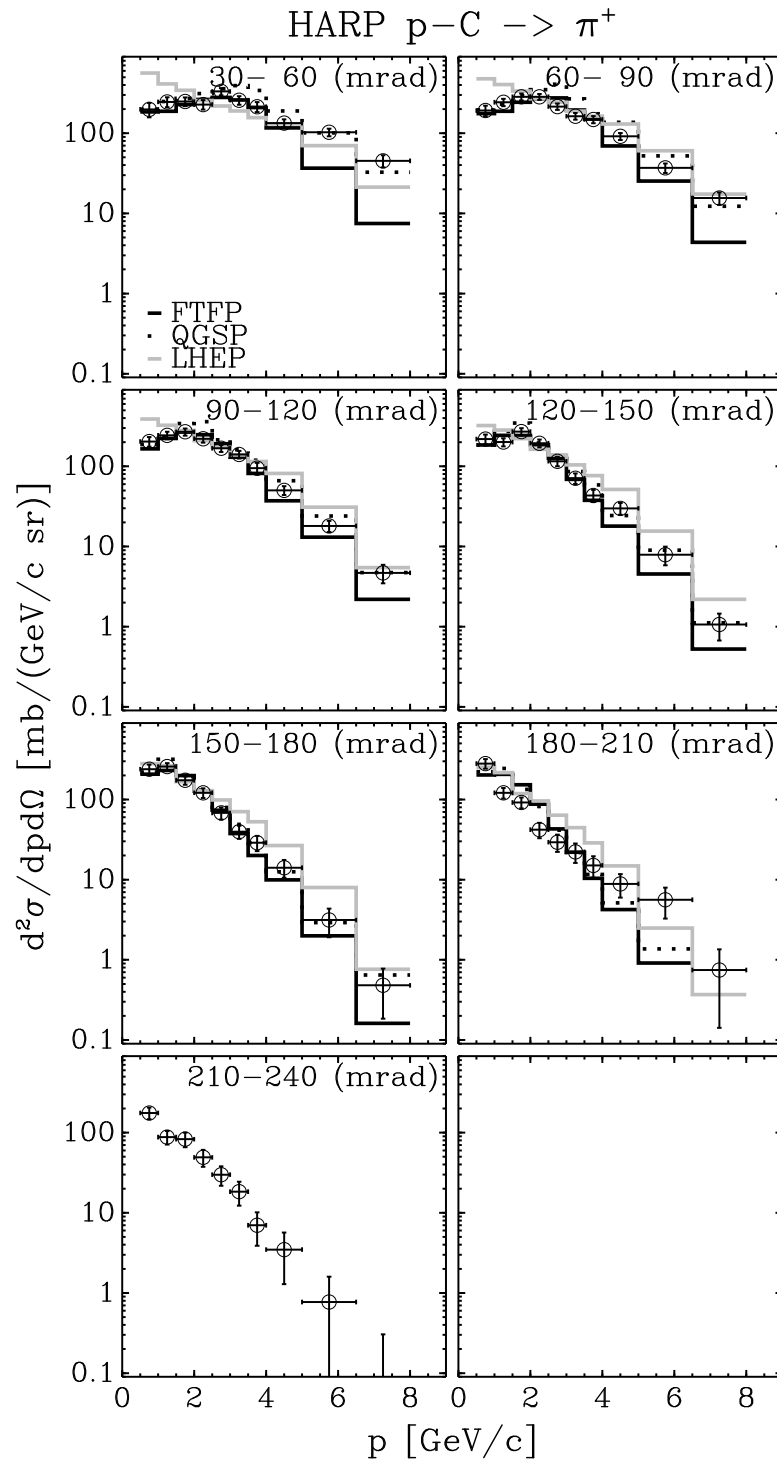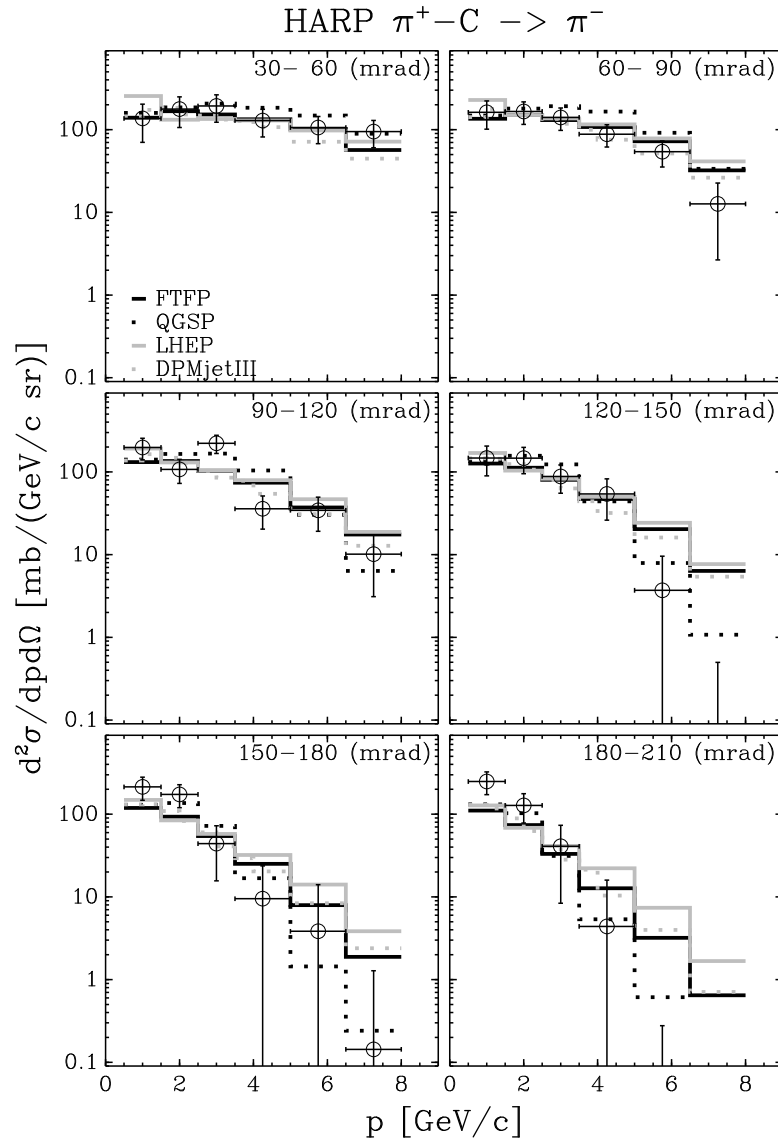
Figure 18: Comparison of the measured double-differential production cross-section of π^+ in π^-–C reactions at 12 GeV/c (points with error bars) with predictions of relevant GEANT4 and DPMJET-III models. Six panels show different angular bins from 30 mrad to 210 mrad (the corresponding angular interval is printed on each panel).
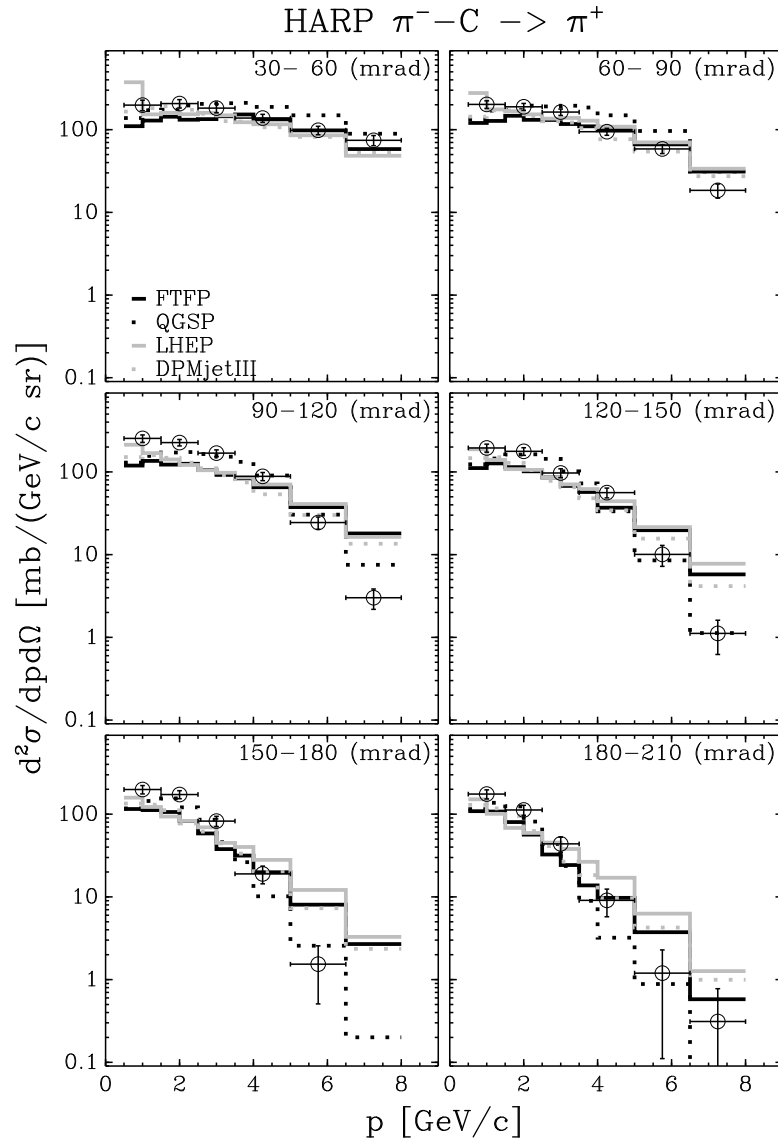
A detailed description of uncertainties in atmospheric neutrino flux calculations due to hadron production can be found in e.g. [44].

Simulations show that collisions of protons with a carbon target are very similar to proton interactions with air. That is why these datasets can be used for tuning models needed in astroparticle physics simulations.

In this paper we presented measurements of the double-differential production cross-section of pions in the collisions of 12 GeV/c protons and charged pions with a carbon 5% nuclear interaction length target. The data were reported in bins of pion momentum and angle in the kinematic range from 0.5 GeV/$c \leq p_\pi < 8$ GeV/c and 0.030 rad $\leq \theta_\pi < 0.240$ rad. A detailed error analysis has been performed yielding integral errors (statistical + systematic) of 6.1% and 7.0% for π^+ and π^- in p-C interactions (10.2% and 8.5% for π^+ and π^- in π^+-C interactions; 6.5% and 8.2% for π^+ and π^- in π^--C interactions) and an overall normalization error of 2% for the proton beam and 3% for the pion beams.

We should stress that the HARP incoming charged pion data are the first precision measurements in this kinematic region.

To check the reliability of hadronic interaction models which are used for air shower simulations, the HARP measurements have been compared to predictions of these models. Our conclusion is that none of the models is able to describe satisfactorily and in detail the measured spectra. Discrepancies are found especially at low and high momenta.

Several models rely on parametrizations of existing accelerator data. Therefore a Sanford-Wang parametrization is given for all measured spectra. The parametrization is, however, not a good description of the data in the full phase space region. From the comparison of the Sanford-Wang fits with model predictions we can conclude that such parametrizations have to be used with caution, especially if these parametrizations are extrapolated to regions where no data are available.

5   Acknowledgments

Table 9: Correlation coefficients among the Sanford-Wang parameters, obtained by fitting the π^+–C and π^-–C datasets.

π^+–C $\rightarrow \pi^-$					
Parameter	c_1	c_2	c_6	c_7	c_8
c_1	1.000				
c_2	-0.680	1.000			
c_6	-0.592	0.891	1.000		
c_7	-0.821	0.199	0.200	1.000	
c_8	-0.445	-0.134	-0.093	0.819	1.000
π^+–C $\rightarrow \pi^+$					
Parameter	c_1	c_2	c_6	c_7	c_8
c_1	1.000				
c_2	-0.753	1.000			
c_6	-0.638	0.909	1.000		
c_7	-0.804	0.263	0.205	1.000	
c_8	-0.129	-0.372	-0.372	0.626	1.000
π^-–C $\rightarrow \pi^-$					
Parameter	c_1	c_2	c_6	c_7	c_8
c_1	1.000				
c_2	-0.765	1.000			
c_6	-0.489	0.796	1.000		
c_7	-0.834	0.374	0.259	1.000	
c_8	-0.240	-0.218	-0.240	0.611	1.000

π^-–C $\rightarrow \pi^+$							
Parameter	c_1	c_2	c_3	$c_4 = c_5$	c_6	c_7	c_8
c_1	1.000						
c_2	-0.584	1.000					
c_3	-0.024	-0.250	1.000				
$c_4 = c_5$	-0.088	-0.254	0.973	1.000			
c_6	-0.545	0.668	-0.018	0.097	1.000		
c_7	-0.849	0.195	0.013	0.077	0.314	1.000	
c_8	-0.429	-0.168	-0.024	0.000	-0.116	0.753	1.000

A   Cross-section data

Table 10: HARP results for the double-differential π^+ and π^- production cross-section in the laboratory system, $d^2\sigma^\pi/(dpd\Omega)$, for p-C interactions at 12 GeV/c. Each row refers to a different ($p_{\min} \leq p < p_{\max}, \theta_{\min} \leq \theta < \theta_{\max}$) bin, where p and θ are the pion momentum and polar angle, respectively. The central value as well as the square-root of the diagonal elements of the covariance matrix are given.

$\theta_{\min}$ (mrad)	$\theta_{\max}$ (mrad)	$p_{\min}$ (GeV/c)	$p_{\max}$ (GeV/c)	$d^2\sigma^{\pi^+}/(dpd\Omega)$ (mb/(GeV/c sr))			$d^2\sigma^{\pi^-}/(dpd\Omega)$ (mb/(GeV/c sr))		
30	60	0.5	1.0	198.5	$\pm$	40.8	135.4	$\pm$	30.5
		1.0	1.5	245.8	$\pm$	35.0	212.5	$\pm$	30.8
		1.5	2.0	248.2	$\pm$	31.1	230.6	$\pm$	32.1
		2.0	2.5	227.9	$\pm$	31.0	113.6	$\pm$	21.9
		2.5	3.0	331.6	$\pm$	34.2	122.6	$\pm$	22.6
		3.0	3.5	258.2	$\pm$	31.4	98.1	$\pm$	18.9
		3.5	4.0	214.1	$\pm$	30.5	82.3	$\pm$	14.8
		4.0	5.0	133.5	$\pm$	15.1	57.5	$\pm$	10.4
		5.0	6.5	102.6	$\pm$	11.0	23.2	$\pm$	6.2
		6.5	8.0	45.2	$\pm$	7.8	5.1	$\pm$	4.3
60	90	0.5	1.0	191.7	$\pm$	29.1	151.3	$\pm$	24.9
		1.0	1.5	243.2	$\pm$	25.4	180.6	$\pm$	22.0
		1.5	2.0	284.9	$\pm$	27.9	191.6	$\pm$	21.3
		2.0	2.5	284.4	$\pm$	24.3	158.2	$\pm$	18.0
		2.5	3.0	214.9	$\pm$	19.8	101.7	$\pm$	14.0
		3.0	3.5	163.1	$\pm$	15.8	85.1	$\pm$	12.0
		3.5	4.0	148.4	$\pm$	15.2	64.5	$\pm$	12.2
		4.0	5.0	91.4	$\pm$	9.3	37.2	$\pm$	5.5
		5.0	6.5	36.9	$\pm$	5.0	12.5	$\pm$	2.8
		6.5	8.0	15.6	$\pm$	2.7	1.8	$\pm$	1.0
90	120	0.5	1.0	204.0	$\pm$	27.8	217.4	$\pm$	31.2
		1.0	1.5	243.7	$\pm$	26.2	204.7	$\pm$	23.2
		1.5	2.0	269.4	$\pm$	27.7	185.1	$\pm$	21.0
		2.0	2.5	221.3	$\pm$	23.4	132.1	$\pm$	16.5
		2.5	3.0	168.0	$\pm$	17.0	91.8	$\pm$	13.8
		3.0	3.5	140.5	$\pm$	15.2	60.5	$\pm$	9.2
		3.5	4.0	94.8	$\pm$	15.6	30.7	$\pm$	5.1
		4.0	5.0	50.2	$\pm$	6.3	24.4	$\pm$	5.2
		5.0	6.5	18.0	$\pm$	2.9	3.1	$\pm$	1.1
		6.5	8.0	4.7	$\pm$	1.2	0.1	$\pm$	0.1

$\theta_{\min}$ (mrad)	$\theta_{\max}$ (mrad)	$p_{\min}$ (GeV/c)	$p_{\max}$ (GeV/c)	$d^2\sigma^{\pi^+}/(dpd\Omega)$ (mb/(GeV/c sr))			$d^2\sigma^{\pi^-}/(dpd\Omega)$ (mb/(GeV/c sr))		
120	150	0.5	1.0	218.8	$\pm$	30.6	230.5	$\pm$	34.5
		1.0	1.5	200.6	$\pm$	23.4	198.9	$\pm$	23.7
		1.5	2.0	271.3	$\pm$	28.5	130.7	$\pm$	17.4
		2.0	2.5	194.3	$\pm$	21.6	79.7	$\pm$	12.7
		2.5	3.0	115.7	$\pm$	15.6	66.7	$\pm$	11.3
		3.0	3.5	71.0	$\pm$	10.7	52.5	$\pm$	9.6
		3.5	4.0	43.4	$\pm$	7.4	24.9	$\pm$	5.2
		4.0	5.0	29.9	$\pm$	5.0	14.0	$\pm$	3.5
		5.0	6.5	7.9	$\pm$	2.1	3.1	$\pm$	1.3
		6.5	8.0	1.1	$\pm$	0.4	0.3	$\pm$	0.2
150	180	0.5	1.0	238.9	$\pm$	34.1	193.4	$\pm$	28.9
		1.0	1.5	257.5	$\pm$	26.9	142.8	$\pm$	20.0
		1.5	2.0	173.7	$\pm$	20.8	137.6	$\pm$	19.3
		2.0	2.5	121.3	$\pm$	16.7	82.1	$\pm$	13.1
		2.5	3.0	67.9	$\pm$	11.8	60.2	$\pm$	11.2
		3.0	3.5	39.7	$\pm$	7.4	27.3	$\pm$	6.2
		3.5	4.0	28.9	$\pm$	6.3	17.9	$\pm$	5.0
		4.0	5.0	14.1	$\pm$	3.5	9.8	$\pm$	3.3
		5.0	6.5	3.1	$\pm$	1.2	0.8	$\pm$	0.7
		6.5	8.0	0.5	$\pm$	0.3		—	
180	210	0.5	1.0	280.1	$\pm$	38.2	242.0	$\pm$	35.1
		1.0	1.5	121.0	$\pm$	18.2	134.0	$\pm$	19.8
		1.5	2.0	91.8	$\pm$	14.2	107.6	$\pm$	16.8
		2.0	2.5	42.0	$\pm$	9.1	63.7	$\pm$	11.9
		2.5	3.0	29.3	$\pm$	7.1	28.4	$\pm$	7.2
		3.0	3.5	22.2	$\pm$	6.1	14.4	$\pm$	4.6
		3.5	4.0	15.1	$\pm$	4.5	7.4	$\pm$	3.4
		4.0	5.0	8.9	$\pm$	2.9	2.0	$\pm$	1.3
		5.0	6.5	5.6	$\pm$	2.3	0.3	$\pm$	0.4
		6.5	8.0	0.7	$\pm$	0.6		—	
210	240	0.5	1.0	175.8	$\pm$	29.2	119.4	$\pm$	21.3
		1.0	1.5	87.9	$\pm$	16.8	85.4	$\pm$	14.9
		1.5	2.0	82.8	$\pm$	17.1	92.6	$\pm$	18.4
		2.0	2.5	49.1	$\pm$	11.7	40.3	$\pm$	10.6
		2.5	3.0	29.9	$\pm$	8.2	15.5	$\pm$	5.4
		3.0	3.5	18.3	$\pm$	6.1	8.7	$\pm$	4.2
		3.5	4.0	7.0	$\pm$	3.1	3.1	$\pm$	2.3
		4.0	5.0	3.5	$\pm$	2.2	1.6	$\pm$	1.6
		5.0	6.5	0.8	$\pm$	0.8	0.2	$\pm$	0.4
		6.5	8.0	0.1	$\pm$	0.2		—	

Table 11: HARP results for the double-differential π^+ and π^- production cross-section in the laboratory system, $d^2\sigma^\pi/(dpd\Omega)$, for π^+-C interactions at 12 GeV/c. Each row refers to a different ($p_{min} \leq p < p_{max}, \theta_{min} \leq \theta < \theta_{max}$) bin, where p and θ are the pion momentum and polar angle, respectively. The central value as well as the square-root of the diagonal elements of the covariance matrix are given.

θ_{min} (mrad)	θ_{max} (mrad)	p_{min} (GeV/c)	p_{max} (GeV/c)	$d^2\sigma^{\pi^+}/(dpd\Omega)$ (mb/(GeV/c sr))			$d^2\sigma^{\pi^-}/(dpd\Omega)$ (mb/(GeV/c sr))		
30	60	0.50	1.50	191.5	$\pm$	85.0	136.7	$\pm$	66.4
		1.50	2.50	173.0	$\pm$	65.1	177.6	$\pm$	71.3
		2.50	3.50	354.0	$\pm$	88.4	193.3	$\pm$	70.2
		3.50	5.00	302.1	$\pm$	63.6	129.0	$\pm$	47.4
		5.00	6.50	177.8	$\pm$	46.9	106.1	$\pm$	38.3
		6.50	8.00	196.8	$\pm$	48.5	94.8	$\pm$	34.4
60	90	0.50	1.50	259.1	$\pm$	70.7	161.9	$\pm$	60.5
		1.50	2.50	337.1	$\pm$	65.8	166.2	$\pm$	50.2
		2.50	3.50	243.0	$\pm$	53.9	140.6	$\pm$	42.4
		3.50	5.00	179.4	$\pm$	37.4	88.2	$\pm$	26.4
		5.00	6.50	149.7	$\pm$	32.9	54.1	$\pm$	18.8
		6.50	8.00	49.7	$\pm$	15.3	12.6	$\pm$	10.0
90	120	0.50	1.50	268.2	$\pm$	64.9	197.6	$\pm$	57.5
		1.50	2.50	332.0	$\pm$	65.3	107.3	$\pm$	34.6
		2.50	3.50	237.4	$\pm$	47.4	222.3	$\pm$	55.1
		3.50	5.00	153.1	$\pm$	34.5	35.8	$\pm$	15.5
		5.00	6.50	60.2	$\pm$	18.9	34.4	$\pm$	15.2
		6.50	8.00	23.0	$\pm$	9.7	10.1	$\pm$	7.0
120	150	0.50	1.50	178.9	$\pm$	54.8	147.4	$\pm$	57.8
		1.50	2.50	264.2	$\pm$	61.8	146.7	$\pm$	51.6
		2.50	3.50	178.2	$\pm$	46.3	88.3	$\pm$	33.0
		3.50	5.00	73.0	$\pm$	26.3	54.3	$\pm$	28.1
		5.00	6.50	31.8	$\pm$	15.5	3.7	$\pm$	5.9
		6.50	8.00	7.8	$\pm$	7.0		—	
150	180	0.50	1.50	181.1	$\pm$	56.3	213.8	$\pm$	66.6
		1.50	2.50	165.7	$\pm$	53.6	173.5	$\pm$	53.7
		2.50	3.50	136.2	$\pm$	44.0	44.0	$\pm$	28.4
		3.50	5.00	25.7	$\pm$	16.0	9.5	$\pm$	14.2
		5.00	6.50	21.3	$\pm$	17.0	3.8	$\pm$	10.2
		6.50	8.00	4.5	$\pm$	7.3		—	
180	210	0.50	1.50	219.0	$\pm$	73.4	248.5	$\pm$	76.1
		1.50	2.50	77.1	$\pm$	35.6	127.8	$\pm$	49.5
		2.50	3.50	81.2	$\pm$	42.1	40.9	$\pm$	32.6
		3.50	5.00	29.6	$\pm$	24.6	4.4	$\pm$	11.6
		5.00	6.50	8.4	$\pm$	13.8	0.0	$\pm$	0.3
		6.50	8.00	0.4	$\pm$	3.0		—	

Table 12: HARP results for the double-differential π^+ and π^- production cross-section in the laboratory system, $d^2\sigma^\pi/(dpd\Omega)$, for π^--C interactions at 12 GeV/c. Each row refers to a different ($p_{min} \le p < p_{max}, \theta_{min} \le \theta < \theta_{max}$) bin, where p and θ are the pion momentum and polar angle, respectively. The central value as well as the square-root of the diagonal elements of the covariance matrix are given.

θ_{min} (mrad)	θ_{max} (mrad)	p_{min} (GeV/c)	p_{max} (GeV/c)	$d^2\sigma^{\pi^+}/(dpd\Omega)$ (mb/(GeV/c sr))			$d^2\sigma^{\pi^-}/(dpd\Omega)$ (mb/(GeV/c sr))		
30	60	0.50	1.50	198.1	$\pm$	28.7	189.6	$\pm$	28.7
		1.50	2.50	206.8	$\pm$	24.2	284.9	$\pm$	31.4
		2.50	3.50	182.0	$\pm$	22.2	263.8	$\pm$	27.1
		3.50	5.00	138.0	$\pm$	15.3	242.0	$\pm$	19.6
		5.00	6.50	98.4	$\pm$	11.4	257.7	$\pm$	22.1
		6.50	8.00	74.4	$\pm$	10.4	260.9	$\pm$	17.4
60	90	0.50	1.50	201.9	$\pm$	21.7	249.0	$\pm$	26.6
		1.50	2.50	189.2	$\pm$	18.1	302.4	$\pm$	24.5
		2.50	3.50	163.1	$\pm$	14.6	247.5	$\pm$	18.8
		3.50	5.00	94.6	$\pm$	9.1	200.3	$\pm$	13.6
		5.00	6.50	58.5	$\pm$	7.1	129.2	$\pm$	9.4
		6.50	8.00	18.4	$\pm$	3.6	81.1	$\pm$	8.2
90	120	0.50	1.50	254.2	$\pm$	26.1	317.1	$\pm$	33.1
		1.50	2.50	226.4	$\pm$	20.4	325.5	$\pm$	27.5
		2.50	3.50	169.0	$\pm$	16.0	263.9	$\pm$	22.0
		3.50	5.00	88.4	$\pm$	10.0	146.9	$\pm$	12.6
		5.00	6.50	24.4	$\pm$	4.1	70.1	$\pm$	7.3
		6.50	8.00	3.0	$\pm$	0.8	29.0	$\pm$	4.3
120	150	0.50	1.50	195.2	$\pm$	21.6	267.8	$\pm$	29.9
		1.50	2.50	177.4	$\pm$	19.0	235.3	$\pm$	22.1
		2.50	3.50	97.1	$\pm$	11.9	159.9	$\pm$	16.6
		3.50	5.00	56.2	$\pm$	7.7	87.1	$\pm$	10.3
		5.00	6.50	10.1	$\pm$	2.8	29.6	$\pm$	5.0
		6.50	8.00	1.1	$\pm$	0.5	8.7	$\pm$	2.3
150	180	0.50	1.50	198.9	$\pm$	23.2	267.8	$\pm$	30.7
		1.50	2.50	173.1	$\pm$	19.3	233.1	$\pm$	23.7
		2.50	3.50	82.6	$\pm$	11.8	89.4	$\pm$	12.0
		3.50	5.00	19.0	$\pm$	4.6	48.9	$\pm$	7.4
		5.00	6.50	1.5	$\pm$	1.0	11.8	$\pm$	2.9
		6.50	8.00		—		3.6	$\pm$	1.3
180	210	0.50	1.50	175.1	$\pm$	22.0	246.9	$\pm$	29.6
		1.50	2.50	112.6	$\pm$	15.5	106.1	$\pm$	14.3
		2.50	3.50	43.7	$\pm$	9.0	51.4	$\pm$	8.7
		3.50	5.00	9.1	$\pm$	3.3	17.2	$\pm$	3.8
		5.00	6.50	1.2	$\pm$	1.1	7.4	$\pm$	2.4
		6.50	8.00		—		2.4	$\pm$	1.0

References

[1] M. G. Catanesi *et al.*, HARP Collaboration, "Proposal to study hadron production for the neutrino factory and for the atmospheric neutrino flux", CERN-SPSC/99-35 (1999).

[2] M. G. Catanesi *et al.* [HARP Collaboration], "The HARP Detector at the CERN PS", Nucl. Instrum. Meth. A **571** (2007) 527.

[3] M. Apollonio *et al.*, "Oscillation Physics with a Neutrino Factory", CERN TH2002-208, [arXiv:hep-ph/0210192];
A. Baldini *et al.*, BENE Steering Group, CERN-2006-005;
A. Blondel *et al.*, CERN-2004-002, ECFA/04/230.

[4] M. Honda, T. Kajita, K. Kasahara and S. Midorikawa, Phys. Rev. D **70** (2004) 043008; Phys. Rev. D **75** (2007) 043005 [arXiv:astro-ph/0611201].
M. Honda, T. Kajita, K. Kasahara, S. Midorikawa and T. Sanuki, Phys. Rev. D **75** (2007) 043006 [arXiv:astro-ph/0611418].
G. D. Barr, T. K. Gaisser, P. Lipari, S. Robbins and T. Stanev, Phys. Rev. D **70** (2004) 023006.
G. Battistoni, A. Ferrari, T. Montaruli and P. R. Sala, [arXiv:hep-ph/0305208]
G. Battistoni, A. Ferrari, T. Montaruli and P. R. Sala, Astropart. Phys. **19** (2003) 269 [Erratum-ibid. **19** (2003) 291]
G. Battistoni, A. Ferrari, P. Lipari, T. Montaruli, P. R. Sala and T. Rancati, Astropart. Phys. **12** (2000) 315

[5] E. Aliu *et al.* [K2K Collaboration], "Evidence for muon neutrino oscillation in an accelerator-based experiment," Phys. Rev. Lett. **94** (2005) 081802 [arXiv:hep-ex/0411038].

[6] M. H. Ahn *et al.* [K2K Collaboration], "Measurement of neutrino oscillation by the K2K experiment", Phys. Rev. D **74** (2006) 072003 [arXiv:hep-ex/0606032].

[7] E. Church *et al.* [BooNe Collaboration], "A proposal for an experiment to measure muon-neutrino → electron-neutrino oscillations and muon-neutrino disappearance at the Fermilab Booster: BooNE", FERMILAB-PROPOSAL-0898.
A. A. Aguilar-Arevalo *et al.* [MiniBooNE Collaboration], arXiv:0704.1500 [hep-ex].

[8] A. A. Aguilar-Arevalo *et al.* [SciBooNE Collaboration], "Bringing the SciBar detector to the Booster neutrino beam", [arXiv:hep-ex/0601022].

[9] M. G. Catanesi *et al.* [HARP Collaboration], "Measurement of the production cross-section of positive pions in p-Al collisions at 12.9 GeV/c", Nucl. Phys. B **732** (2006) 1 [arXiv:hep-ex/0510039].

[10] M. G. Catanesi *et al.*, [HARP Collaboration], "Measurement of the production cross-section of positive pions in the collision of 8.9 GeV/c protons on beryllium", Eur. Phys. J. C **52** (2007) 29 [arXiv:hep-ex/0702024].

[11] M. G. Catanesi *et al.* [HARP Collaboration], "Particle identification algorithms for the HARP forward spectrometer", Nucl. Instrum. Meth. A **572** (2007) 899.

[12] M. G. Catanesi *et al.*, [HARP Collaboration], "Measurement of the Production of charged Pions by Protons on a Tantalum Target", Eur. Phys. J. C **51** (2007) 787, arXiv:0706.1600 [hep-ex].

[13] M. G. Catanesi *et al.*, [HARP Collaboration], "Large-angle production of charged pions by 3 GeV/c– 12 GeV/c protons on carbon, copper and tin targets", Eur. Phys. J. C **53** (2008) 177, arXiv:0709.3464 [hep-ex].

[14] M. G. Catanesi *et al.*, [HARP Collaboration], "Large-angle production of charged pions by 3 GeV/c–12.9 GeV/c protons on beryllium, aluminium and lead targets", arXiv:0709.3458 [hep-ex], to be published in European Physical Journal C.

[15] W. F. Baker *et al.*, Phys. Rev. Lett. **7** (1961) 101.

[16] D. Dekkers *et al.*, Phys. Rev. **137** (1965) B962.

[17] J. V. Allaby *et al.*, CERN Yellow Report 70-12, 1970.

[18] Y. Cho *et al.*, Phys. Rev. D **4** (1971) 1967.

[19] T. Eichten *et al.*, Nucl. Phys. B **44** (1972) 333.

[20] D. Antreasyan *et al.*, Phys. Rev. D **19** N3 (1979) 764.

[21] I. Chemakin *et al.* [E910 Collaboration], Phys. Rev. C **77** (2008) 015209, arXiv:0707.2375 [nucl-ex].

[22] D. S. Barton *et al.*, Phys. Rev. D **27** (1983) 2580.

[23] C. Alt *et al.* [NA49 Collaboration], Eur. Phys. J. C **49** (2007) 897 [arXiv:hep-ex/0606028].

[24] H. Meyer [MIPP Collaboration], J. Phys. Conf. Ser. **69** (2007) 012025.
R. Raja, Nucl. Instrum. Meth. A **553** (2005) 225 [arXiv:hep-ex/0501005].

[25] N. Antoniou *et al.* [NA61 Collaboration], "Study of hadron production in hadron nucleus and nucleus nucleus collisions at the CERN SPS", CERN-SPSC-P-330, CERN-SPSC-2006-043, CERN-SPSC-2007-004, CERN-SPSC-2007-019.

[26] M. Anfreville *et al.*, "The drift chambers of the NOMAD experiment", Nucl. Instrum. Meth. A **481** (2002) 339 [arXiv:hep-ex/0104012].

[27] M. Baldo-Ceolin *et al.*, "The Time-Of-Flight TOFW Detector Of The HARP Experiment: Construction And Performance", Nucl. Instrum. Meth. A **532** (2004) 548.

[28] L. Durieu, A. Mueller and M. Martini, PAC-2001-TPAH142 *Presented at IEEE Particle Accelerator Conference (PAC2001), Chicago, Illinois, 18-22 Jun 2001*;
L. Durieu *et al.*, Proceedings of PAC'97, Vancouver, (1997);
L. Durieu, O. Fernando, CERN PS/PA Note 96-38.

[29] K. Pretzl *et al.*, Invited talk at the "International Symposium on Strangeness and Quark Matter", Crete, (1999) 230.

[30] A. Grossheim, "Particle production yields induced by multi-GeV protons on nuclear targets", Ph.D. thesis, University of Dortmund, Germany, 2003, CERN-THESIS-2004-010.

[31] S. Agostinelli *et al.* [GEANT4 Collaboration], "GEANT4: A simulation toolkit", Nucl. Instrum. Meth. A **506** (2003) 250.

[32] G. D'Agostini, DESY 94-099, ISSN 0418-9833, 1994.
G. D'Agostini, Nucl. Instrum. Meth. A **362** (1995) 487.

[33] Christine Meurer, "Muon production in extensive air showers and fixed target accelerator data", Ph.D. thesis, Karlsruhe, Germany, 2007, CERN-THESIS-2007-078.

[34] V. Blobel and E. Lohrmann, "Statistische und numerische Methoden der Datenanalyse", Stuttgart: Teubner, 1998, ISBN 3-519-03243-0.

[35] M. Kliemant, B. Lungwitz, and M. Gazdzicki, Phys. Rev. C **69** (2004) 044903.

[36] D. Heck *et al.*, Report FZKA 6019 (1998)

[37] J. R. Sanford and C. L. Wang, "Empirical formulas for particle production in p-Be collisions between 10 and 35 BeV/c", Brookhaven National Loboratory, AGS internal report (1967).

[38] H. Fesefeldt, report PITHA-85/02, RWTH Aachen, 1985.

[39] M. Bleicher *et al.*, J. Phys. G: Nucl. Part. Phys. 25 (1999) 1859.

[40] S. Roesler, R. Engel, and J. Ranft, in Proc. of Int. Conf. on Advanced Monte Carlo for Radiation Physics, Particle Transport Simulation and Applications (MC 2000), Lisbon, Portugal, 23-26 Oct 2000, A. Kling, F. Barao, M. Nakagawa, L. Tavora, P. Vaz eds., Springer-Verlag Berlin, p. 1033-1038 (2001), 2000.

[41] G. Folger and H. P. Wellisch, String parton models in Geant4, CHEP'03 (La Jolla, California, USA, 24-28 March 2003); Preprints CHEP-2003-MOMT007, e-Print physics/0306007

[42] D. H. Wright, T. Koi, G. Folger, V. Ivanchenko, M. Kossov, N. Starkov, A. Heikkinen and H. P. Wellisch, 2007 AIP Conf. Proc. 896 11

[43] D. H. Wright, T. Koi, G. Folger, V. Ivanchenko, M. Kossov, N. Starkov, A. Heikkinen and H. P. Wellisch, 2006 AIP Conf. Proc. 867 479

[44] G. D. Barr, T. K. Gaisser, S. Robbins and T. Stanev, Phys. Rev. D **74** (2006) 094009 [arXiv:astro-ph/0611266].